A novel fluoro-electrochemical technique for classifying diverse marine nanophytoplankton

Samuel Barton[1][*], Minjun Yang[2], Haotian Chen[2], Christopher Batchelor-McAuley[2, 3], Richard G. Compton[2], Heather A. Bouman[1], Rosalind E.M. Rickaby[1]

[1] Department of Earth Sciences, University of Oxford, South Parks Road, Oxford, OX1 3AN, UK

[2] Physical and Theoretical Chemistry Laboratory, Department of Chemistry, University of Oxford, South Parks Road, Oxford, OX1 3QZ, UK

[3] School of Chemistry, Trinity College Dublin, Dublin 2, Ireland

* Corresponding author: samuel.barton@earth.ox.ac.uk

A novel fluoro-electrochemical technique for classifying diverse marine nanophytoplankton

Samuel Barton[1*], Minjun Yang[2], Haotian Chen[2], Christopher Batchelor-McAuley[2, 3], Richard G. Compton[2], Heather A. Bouman[1], Rosalind E.M. Rickaby[1]

[1] Department of Earth Sciences, University of Oxford, South Parks Road, Oxford, OX1 3AN, UK

[2] Physical and Theoretical Chemistry Laboratory, Department of Chemistry, University of Oxford, South Parks Road, Oxford, OX1 3QZ, UK

[3] School of Chemistry, Trinity College Dublin, Dublin 2, Ireland

* Corresponding author: samuel.barton@earth.ox.ac.uk

Abstract

To broaden our understanding of pelagic ecosystem responses to environmental change, it is essential that we improve the spatio-temporal resolution of *in situ* monitoring of phytoplankton communities. A key challenge for existing methods is in classifying and quantifying cells within the nanophytoplankton size range (2-20µm). This is particularly difficult when there are similarities in morphology, making visual differentiation difficult for both trained taxonomists and machine learning based approaches. Here we present a rapid fluoro-electrochemical technique for classifying nanophytoplankton, and using a library of 52 diverse strains of nanophytoplankton we assess the accuracy of this technique based on two measurements at the individual level: charge required to reduce per cell chlorophyll *a* fluorescence by 50%, and cell radius. We demonstrate a high degree of accuracy overall (92%) in categorising cells belonging to widely recognised key functional groups, however this is reduced when we consider the broader diversity of "nano-phytoflagellates". Notably, we observe that some groups, for example calcifying *Isochrysidales*, have much greater resilience to electrochemically driven oxidative conditions relative to others of a similar size, making them more easily categorised by the technique. The findings of this study present a promising step forward in advancing our toolkit for monitoring phytoplankton communities. We highlight that, for improved categorisation accuracy, future iterations of the method can be enhanced by measuring additional predictor variables with minimal adjustments to the set-up. In doing so, we foresee this technique being highly applicable, and potentially invaluable, for *in situ* classification and enumeration of the nanophytoplankton size fraction.

Introduction

The essential role that phytoplankton play in sustaining marine ecosystems and driving key biogeochemical cycles, notably the biological carbon pump, is unequivocal. As we progress through the Anthropocene, the oceans are facing unprecedented rates of environmental change. In order to improve our global understanding of the impacts that such change is having on phytoplankton communities, and how this might impact key ecosystems services, we must advance our ability to monitor phytoplankton community structure, both spatially and temporally. It is pertinent that *in situ* measurements can capture and quantify the abundance of dominant functional groups of phytoplankton that are present (*i.e.* groups with different biogeochemical and/or ecological functions), as this can inform us about the likely implications of environmental change for marine food webs, biogeochemical cycles, and the capacity of such communities to contribute to sequestration of dissolved CO_2. Widely recognised functional groups, include (but are not limited to): coccolithophores, diatoms, dinoflagellates, and cyanobacteria (Anderson 2005; Nair et al. 2008; Anderson et al. 2021).

An important consideration when attempting to quantitatively assess *in situ* phytoplankton communities is that, as single unicellular organisms, phytoplankton can exhibit a large variation in size, spanning over four orders of magnitude; ranging in length from picophytoplankton <2µm (including most cyanobacteria and picoeukaryotes) to the largest diatoms >1000µm (Snoeijs et al. 2002; Finkel et al. 2010). From an ecological perspective, size is considered a master trait and is known to significantly influence growth rates, nutrient requirements, grazing susceptibility, and sinking rates (Litchman and Klausmeier 2008); all of which have a bearing on important biogeochemical cycles. In this respect, it has been demonstrated that eukaryotic unicells in the nanophytoplankton size range (2-20µm) display the greatest mass-specific metabolic rates, and thus growth rates, relative to larger microphytoplankton (20µm- 2000µm) and smaller picophytoplankton (Marañón et al. 2013; López-Sandoval et al. 2014; Ward et al. 2017), making them highly competitive and fast responding to environmental perturbations. Indeed, the general success of nanophytoplankton and their ability to dominate phytoplankton biomass has been widely demonstrated from field-based measurements in both the open-ocean (Tarran et al. 2006; Balzano et al. 2012; de Vargas et al. 2015; Bolaños et al. 2020) and coastal waters (Pinckney et al. 2015; Barnes et al. 2015; Alves-De-Souza et al. 2017; Leblanc et al. 2018; Piwosz 2019). Subsequently, as sentinels of the phytoplankton assemblage, nanophytoplankton are an insightful target area for monitoring phytoplankton ecological and biogeochemical functioning in response to ocean change. To date, however, there are numerous constraints and limitations to the available methods in obtaining *in situ* time series measurements of nanophytoplankton diversity and abundance.

Arguably, the most accurate method for quantifying phytoplankton abundance is microscope taxonomy. If specifically focussing on the nanophytoplankton size fraction, taxonomists can quantify abundance to the genus and species level when there are easily identifiable cell characteristics or morphologies (*e.g.* the unique extracellular calcite structures of coccolithophores, or the complex silica frustules of

91   diatoms). However, this size fraction also contains a large proportion of cell types (typically between 2

92   and 10µm) that are extremely hard to identify due to their similar morphology and lack of external

93   inorganic structure (Widdicombe et al. 2010; Piwosz 2019). As a result, a significant proportion of the

94   nanophytoplankton fraction is often given the blanket label of 'nano-phytoflagellates' (or similar) in

95   taxonomy surveys. For example, a long-term time series (> 15 years) of the pelagic phytoplankton

96   communities at the L4 station in the Western English Channel has consistently observed that these

97   'nano-phytoflagellates' make up >80% of the total cell counts per unit volume (Widdicombe et al.

98   2010). The other main limitations of traditional microscopy are that it is time-consuming in nature,

99   requires highly skilled labour input, and live samples being fixed and preserved prior to analysis.

100   Flow cytometry is a higher throughput quantitative approach that is often used to distinguish

101   nanophytoplankton and picophytoplankton size fractions, of either live or fixed samples. Light

102   scattering and autofluorescence detection allow for clustering of cells with similar optical properties.

103   This gives a high degree of separation within the picophytoplankton size fraction, as the cyanobacteria

104   autofluorescence and scattering signal is distinct from that of picoeukaryotes (Collier 2000). Where

105   cytometry falls short is at being able to fully characterise ecologically relevant components of the

106   nanophytoplankton fraction; only coccolithophores (detectable due to their unique light scattering) and

107   cryptophytes (due to their phycoerythrin content) can be discriminated from other nanoeukaryotes

108   (Tarran et al. 2006; Tarran and Bruun 2015). Thus, in order to obtain a true representation of the species

109   present in the nanophytoplankton fraction, previous studies have often complemented microscope

110   taxonomy and cytometry analyses with genetics-based interpretations (Balzano et al. 2012; Leblanc et

111   al. 2018; Piwosz 2019; Bolaños et al. 2020; Stern et al. 2023), which generally only provide a value for

112   relative abundances.

113   Over the last decade or so, there has been an increased application of rapid throughput imaging flow

114   cytometry (Lombard et al. 2019). This technique demonstrates a high degree of accuracy in classifying

115   phytoplankton cell types from a combination of image-based machine learning and autofluorescence

116   measurements (Olson and Sosik 2007; Sosik and Olson 2007; Dugenne et al. 2014; Álvarez et al. 2014;

117   Camoying and Yñiguez 2016; Fragoso et al. 2019; Irisson et al. 2022; Fuchs et al. 2022; Kraft et al.

118   2022); thereby, in essence, merging the identification skills of a microscope taxonomist, with the speed

119   and tools of a flow cytometer. The FlowCam (Yokogawa Fluid Imaging Technologies, Inc) is a

120   laboratory-based device (Sieracki et al. 1998), that has been shown to produce highly comparable results

121   when validated alongside traditional microscopical estimates (Álvarez et al. 2014) and, depending upon

122   the FlowCam model, can analyse a broad range of particle sizes from 300nm to 1mm. As with

123   microscope techniques however, the current models of FlowCam still struggle to classify

124   nanophytoplankton cells that have similar sizes and morphologies. Like FlowCam, the CytoSense

125   (CytoBuoy b.v.) is a non-submersible imaging flow cytometry device that has also performed well

126   alongside traditional microscope taxonomy, but validation is poor for classifying cells that are <5µm in

127 size (Haraguchi et al. 2017). The Imaging FlowCytobot, or IFCB (McClane Research Laboratories,
128 Inc), and CytoBuoy (CytoBuoy b.v.) are devices that operate similarly to those above, but have been
129 developed to function autonomously at sea (Dubelaar et al. 1999; Olson and Sosik 2007; Fragoso et al.
130 2019). These are promising steps forward for the generation of *in situ* spatio-temporal data for
131 monitoring phytoplankton community structure. Indeed, a recent study has shown strong correlation
132 between IFCB measurements and microscopy data for quantifying blooms of filamentous cyanobacteria
133 in the Baltic Sea (Kraft et al. 2021). Nonetheless, whilst the imaging of these devices covers a broad
134 size range, with the IFCB imaging between 10 and 150µm and the CytoBuoy from 1µm to 778µm, both
135 devices are reported to have poor resolution at their lower detection limits necessary for categorising
136 and quantifying nanophytoplankton (Dugenne et al. 2014; Fragoso et al. 2019; Bolaños et al. 2020;
137 Chase et al. 2020; Fuchs et al. 2022). Furthermore, despite advancements in the machine learning
138 techniques used to improve the classification of data obtained from such devices (Fuchs et al. 2022;
139 Kraft et al. 2022), this is only as good as the resolution of the images acquired and the human
140 interpretation that drives the training (Irisson et al. 2022). This presents a substantial challenge in the
141 nanophytoplankton size range, where there are constraints on image resolution at the finer scale
142 (dependant on the objective lens and camera technology employed), along with human limitations in
143 validating (not all nanophytoplankton are easily distinguishable due to similar size and morphology).
144 We therefore identify that a key frontier in monitoring the health of pelagic ecosystems is in developing
145 novel high-throughput techniques that allow for higher resolution *in situ* discrimination and
146 quantification in the nanophytoplankton size range.

147

148 Moving forward, recent developments in the field of analytical chemistry have shown that
149 electrochemically induced oxidative stress destroys phytoplankton chlorophyll *a* fluorescence in a
150 manner that is idiosyncratic, allowing for differentiation of phytoplankton species from measurements
151 that are obtained within 10s of seconds (Yang et al. 2019; Yu et al. 2022).   When a sufficiently high
152 potential is applied to an electrode that is immersed in seawater, a wide range of oxidants can form and
153 diffuse from the electrode surface, for example; oxidation of water to hydrogen peroxide and hydroxyl
154 radicals, bromide to hypobromous acid, and chloride to dichlorine (Yang et al. 2019; Yu et al. 2022).
155 The subsequent reaction of these oxidants with phytoplankton is seen to cause a rapid decay of the
156 cellular chlorophyll *a* fluorescence signal. The rate at which this happens is dependent on a number of
157 factors, including; the distance of the phytoplankton cells from the electrode, the potential applied (and
158 thus the species and concentration of oxidants generated), and more importantly for the work presented
159 here – the type of phytoplankton cell.   To that end, we apply this novel fluoro-electrochemical method
160 to a much broader suite of ecologically relevant pico- and nanophytoplankton (52 cultured strains) to
161 produce a 'susceptibility library' based on two variables; chlorophyll *a* fluorescence 'switch-off' and
162 measured cell radius. This library is assessed using a random forest approach to determine how well the

163 electrochemical method can be used to classify cells into relevant groups. We specifically focussed on
164 strains of nanophytoplankton that (a) represent key functional groups and (b) represent some of the
165 traditionally hard to identify "nano-phytoflagellates". We then explore a possible biological
166 underpinning to the method, as well as discussing its current limitations and suggested improvements.

167

Methods and Procedures

169

Culturing for the 'susceptibility library'

171 Phytoplankton monocultures were selected so that we had a good representation of each of the key
172 functional groups (5 groups, represented by 37 strains in total), along with an assortment of strains that
173 we consider to be likely 'nano-phytoflagellate' candidates (6 groups, represented by 15 strains in total,
174 within the 2 to 10µm size range). The key functional groups that we analyse are herein labelled as:
175 "Calcifying Isochrysidales" (7 strains), "Coccolithophores" (8 strains), "Diatoms" (10 strains),
176 "Dinoflagellates" (8 strains), and "Picophytoplankton" (4 strains). In this instance, "Calcifying
177 Isochrysidales" includes strains of both *Emiliania huxleyi* (7 strains) and *Gephyrocapsa oceanica* (1
178 strain). Whilst they might both be considered coccolithophores, given their cosmopolitan nature and the
179 fact they are the most globally abundant calcifiers (particularly *E. huxleyi*) we considered them as a
180 separate group for this analysis. We also chose to include a range of *E. huxleyi* cell stages (both calcified
181 and non-calcified diploid strains, along with a haploid strain) and morphologies (representing different
182 extents of calcification), allowing us to robustly investigate the within species variance in the
183 electrochemical susceptibility. Picophytoplankton are included to allow us to test the lower size limits
184 for detection and classification of our method, including two strains of cyanobacteria (both
185 *Synechococcus* sp.) and two pico-eukaryotes (*Micromonas pusilla* and *Ostreococcus tauri*). Broadening
186 the dataset to encompass nanophytoplankton beyond the key functional groups, the additional groups
187 in our analysis were as follows: "Eustigmatales" (1 strain), "Green algae" (3 strains), "Non-calcifying
188 Isochrysidales" (4 strains), "Pavlovales" (3 strains), "Phaeocystales" (1 strain), and Prymnesiales (3
189 strains). These strains were selected as it has previously been noted that the unrecognisable "nano-
190 phytoflagelletes", which are a challenge for microscope taxonomy, could broadly be assigned to the
191 phyla of haptophytes (non-calcified types), chlorophytes (or green algae), and cryptophytes (Piwosz
192 2019). A full list of the 52 strains used in this study can be found in SI Table S1. In the case of
193 "Eustigmatales" we assume that a single strain of *Nannochloropsis granulata* is broadly representative,
194 and for "Phyaeocystales" we worked with a single strain of *Phaeocystis globosa*.

195 All strains were obtained from reputable culture collections: Roscoff Culture Collection (Roscoff,
196 France), Culture Collection of Algae and Protozoa (Oban, UK) and The Marine Biological Association
197 (Plymouth, UK). Following their arrival, they were maintained in exponential growth through regular

198 sub-culturing under sterile conditions on their advised growth medium (see Table S1, SI). All growth
199 media were prepared using synthetic ocean water (Morel et al. 1979), allowing greater control over the
200 main composition of the seawater (see Table S2, SI), and thus consistency in the probable oxidants
201 formed when measuring the electrochemical responses (note: a negligible effect of growth medium on
202 the susceptibility to the electrochemical stress was observed when compared alongside natural seawater,
203 see Fig. S3, SI). Cultures were incubated in PHCbi MLR-352-PE Incubators (PHC Europe B.V.) set to
204 17ºC (or 20 ºC for all diatoms), with a 14:10h light-dark regime at a PAR intensity of 20-40μmol m^{-2}
205 s^{-1}, and were kept under these conditions for a minimum of two months prior to carrying out the
206 electrochemical susceptibility measurements. The growth of the cultures was tracked on a daily basis
207 using a TECAN Spark plate reader (Tecan Group Ltd.), where three technical replicates of 200μl of
208 each culture were measured for chlorophyll *a* fluorescence as a proxy for culture biomass. We then
209 selected a time-point in mid-exponential growth phase, when each strain was not at saturation point (*i.e.*
210 carrying capacity) and therefore not nutrient limited, to conduct our experiments (see Figure S1, SI);
211 however, for a couple of strains, susceptibility measurements were taken at different growth phases
212 (and thus different nutrient availability) and only a minimal difference was observed across the phases
213 (see Fig. S4, SI). Immediately prior to the electrochemical experiments, to obtain a sufficient number
214 of cells per image series (as described below), all strains were concentrated by centrifugation
215 (Centrifuge 5702, Eppendorf UK Limited) at 1000 r.p.m for ten minutes, and resuspended to a
216 concentration typically ranging between 5 and 10x.

217

218 The fluoro-electrochemical technique

219 A more detailed description of the fundamental electrochemical principles and details of the underlying
220 methodology, including specifics of the equipment used, can be found in the previously published work
221 by Yu *et al.* (2022). For the purposes of this study, the step-by-step method described below outlines
222 the essential procedures that were followed to yield the underlying dataset for the susceptibility library.
223 In summary, we used a galvanostat based ramping linear current, applied to phytoplankton cells settled
224 onto the surface of a carbon electrode (thus controlling for distance from the electrode) and monitored
225 chlorophyll *a* fluorescence decay over time per individual cell (see Table S3 for number of individual
226 cell measurements per strain). The constant rate of current ramping (10μA s^{-1}) means that the moles of
227 oxidant being generated electrochemically increases with time in a controlled fashion. This approach
228 allows for greater possible discrimination of phytoplankton cell types and over a shorter experimental
229 time frame (e.g. 10s of seconds), as opposed to running experiments at a single set potential.
230 Consequently, as cell types have different levels of resilience to such oxidative stress, this technique
231 enables us to quantify the differences in time that is required to drive the chlorophyll *a* quenching across
232 the phytoplankton investigated.
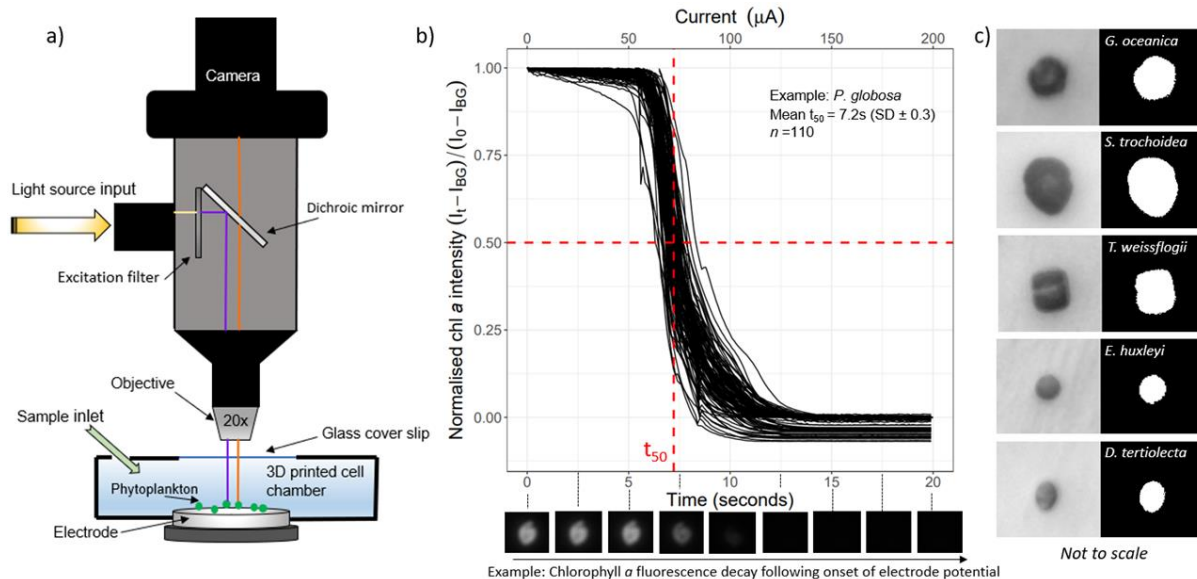
Figure 1. **(a)** a simple schematic diagram of the electrochemistry – fluorescence microscope set up adapted from Yu *et al.* (2022), **(b)** an example of normalised Chlorophyll *a* fluorescence transient data for the species *Phaeocystis globosa*, following onset of the potential (at time 0 seconds) and with a current ramping of $10\mu A\ s^{-1}$. Each black line represents a single cell measurement ($n = 110$), and the dashed red markings highlight the time point, t_{50}, where normalised fluorescence values have been reduced by 50%. The time-series of images below the plot illustrate the loss of fluorescence with time for one individual cell. **(c)** examples of brightfield images taken before the electrochemical experiments for a selection of strains (left column), and the respective estimate of projected pixel area that was subsequently used to determine the effective radius of each cell (after assuming a circular shape).

The fluoro-electrochemical measurements were made as follows (See Fig. 1a, adapted from Yu *et al.* 2022).

1) A concentrated sample from a phytoplankton monoculture in exponential growth phase (as described in Culturing section above) was 'drop cast' onto the surface of the working electrode. After ~1 minute of allowing the cells to be deposited on the surface, excess solution was gently drawn-off using a tissue. Immediately following this, the 3D printed cell chamber was filled up to maximum capacity with culture growth medium via the sample inlet. Once the chamber was at capacity a glass cover slip was put in place.

2) Using the fluorescence microscope (Axio Examiner, Carl Zeiss Ltd., Cambridge U.K.), we focussed on a field of view whereby we had a high proportion of phytoplankton cells on the electrode surface (mean number per experiment $= 23 \pm 18$ S.D., across 212 unique experimental image series).

3) With the microscope set in bright-field mode, we took an image of the starting positioning of the cells. These images were later used to obtain an estimate of effective cell radius (see Fig. 1c).

4) Next, switching the microscope to fluorescence mode, the cells were excited using a $475 \pm 35nm$ excitation filter and emission signal passed through a dichroic mirror specific to

8

261   wavelengths >590nm for chlorophyll *a* fluorescence detection. Simultaneously, the

262   galvanostatic control was synchronised with the camera and data acquisition was started. For

263   the first 40s of the electrochemical experiment no potential was applied, allowing the

264   fluorescence signal to stabilise. Following this, the current was ramped from 0μA at a rate of

265   10μA s^{-1} and images recorded at a capture rate of 10f.p.s. For each set of experiments the current

266   was ramped until the chlorophyll signal had completely 'switched off'.

267   5) After the experiment, the 3D chamber was rinsed clean with DI water and the above steps were

268   repeated a minimum number of 3 times for each phytoplankton strain.

269 Following the experimental data collection, the raw fluorescence transient data was processed for each

270 individual cell within each experimental time-series ($n = 4884$, across all strains) using ImageJ software

271 (v1.53c, Fiji distribution), where "n" is the number of individual phytoplankton cell measurements. The

272 integrated fluorescence intensity values for each individual cell (I_t) were corrected by subtracting the

273 background signal of the electrode surface (I_{BG}) for all time points: $I_t - I_{BG}$, following this all values were

274 then normalised by dividing by the fluorescence intensity at the onset of the potential (I_0): ($I_t - I_{BG}$) / (I_0

275 $- I_{BG}$). We then used the normalised transient data to determine the time-point for each individual cell

276 where normalised intensity had decreased by 50% (t_{50}), see Fig. 1b. Due to the consistent linear ramping

277 of current at 10μA s^{-1} and that all phytoplankton cells imaged were settled on the surface of the electrode

278 within the timescale of the experiments, we were able to determine the total charge required to be

279 injected to reach t_{50} for each cell, and thus we herein refer to our chlorophyll *a* susceptibility factor as

280 charge at t_{50} (in mC). In some instances where there was significant movement of individual cells it was

281 not possible to accurately measure the chlorophyll *a* fluorescence profile throughout the time series,

282 and subsequently data for these cells was considered erroneous and removed from the analysis.

283 For each cell specific chlorophyll *a* fluorescence transient, we used the corresponding bright-field image

284 collected prior to electrochemical experiments to derive a corresponding cellular area based on white

285 pixel area of the cell (Fig. 1c). This was achieved by using the auto-threshold function in ImageJ

286 freeware. From the total pixel area and using a predefined μm to pixel ratio (0.31μm per pixel), we were

287 able to estimate an effective radius (in μm) of each cell by assuming a circular 2D cell geometry (or a

288 spherical cell). For cells in the picophytoplankton size range, due to the lack of contrast with the

289 electrode surface it was not possible to accurately distinguish cell area, and therefore in these instances

290 we obtained a measurement of mean cell pixel area by manually measuring the area of a subset of at

291 least 10 cells per experimental time-series (using ImageJ).

292

293

294

295 **Assessment of the susceptibility library**

With the two parameters of charge at t_{50} (mC) and effective radius (µm) defined for each individual cell, we assessed the applicability of the susceptibility library for distinguishing the cells into pre-defined groupings of relevance, as defined in the Culturing section above. Prior to this assessment it was necessary to balance the dataset for even strain representation within each pre-defined grouping. This was necessary as there was limited control over the number of individual cell transients obtained per experimental image series per strain (due to unpredictable numbers of cells depositing on the electrode surface), resulting in under/over-representation within groups (see Table S3, SI). To balance the data at the group level, we identified the strain within each group that had the lowest number of observations, and used that minimum number to randomly subset a sample of the same length for each of the other strains within the grouping level. This was achieved using the "*sample_n*" function in the R package "*dplyr*" (R version 4.2.2). The resultant balanced dataframe ($n = 2277$) was subsequently used to derive mean values at the group level and for the analyses described below (see Tables S4 and S5 for balanced data, SI).
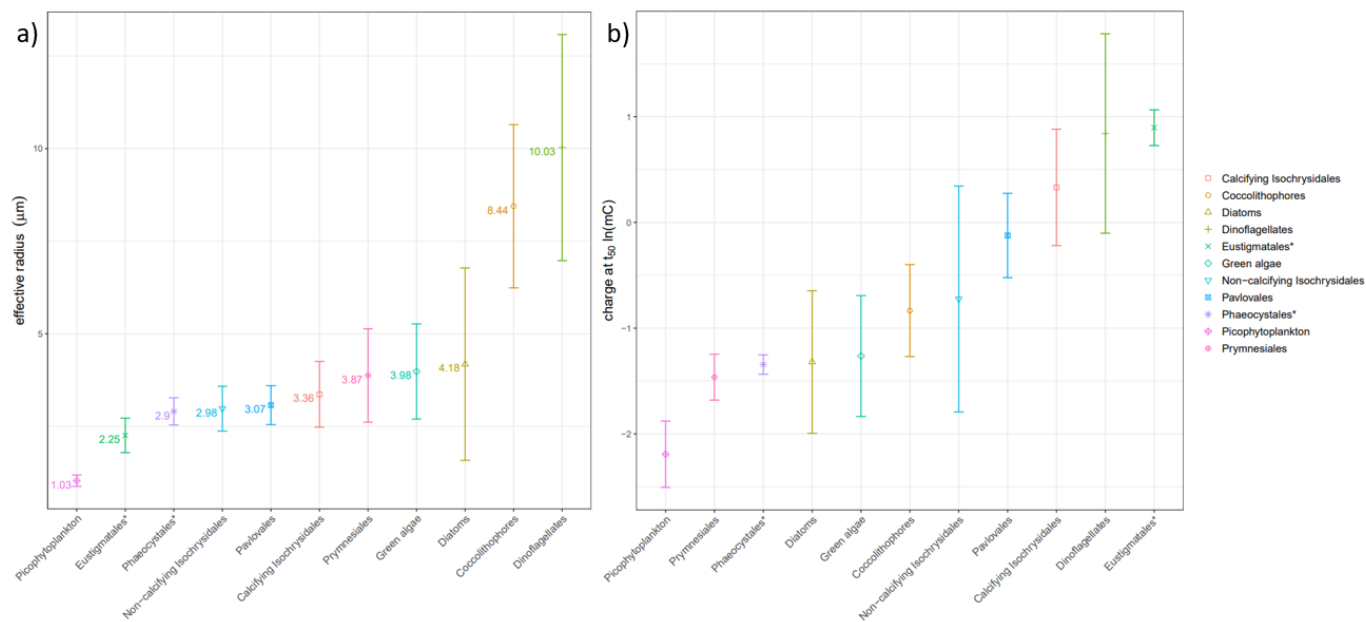
Figure 2. **(a)** Mean effective radius (µm) at the level of each phytoplankton grouping defined in this study. The numbers alongside respective datapoints are the mean effective radius in µm. **(b)** Natural logarithm converted mean charge at t_{50} (mC) for each phytoplankton grouping. Data points represent the mean for each group, and error bars represent the standard deviation of the mean (see Table S5). Colour coding and shapes represent each group (see legend). Note: the ordering on the *x*-axis is in ascending order for each plot, demonstrating that across the groups larger cell radius does not necessarily result in greater charge at t_{50}.

First, looking at charge at t_{50} independently from radius, across all strains we see a large range spanning three orders of magnitude (see Table S4, SI), from a mean of 0.08mC (±0.02 S.D.) for the pico-

321   eukaryote *Ostreococcus tauri*, up to 7.34mC (±1.88 S.D.) for the dinoflagellate *Scripsiella trochoidea*.

322   At the level of the pre-defined groupings described above we see the lowest mean charge at t_{50} within

323   the "Picophytoplankton" of 0.11mC (±0.03 S.D.), and the greatest mean charge at t_{50} within the

324   "Eustigmatales" 2.45mC (±0.41 S.D.), preceded by "Dinoflagellates" at 2.32mC (±2.22 S.D.) (see Fig.

325   2b and Table S5, SI). The large range in these values indicate that there is a strong effect of cell grouping

326   on the resilience to electrochemically driven oxidative stress. Critically, however, there is also

327   considerable overlap in the values, as an example: "Calcifying Isochrysidales" have a mean charge at

328   t_{50} of 1.39mC (±0.57 S.D.), which sits well within the large deviation range of the "Dinoflagellates".

329   Subsequently, in order to further distinguish the groupings in such instances, use of the effective radius

330   can provide an additional dimension for separation where there is overlap. In the case of the previous

331   example, we see that "Calcifying Isochrysidales" have a mean effective radius of 3.36μm (±0.89 S.D.),

332   whereas "Dinoflagellates" have a significantly larger mean effective radius of 10.03μm (±3.05 S.D.)

333   (see Fig. 2a and Table S5, SI). Taking this forward, we next use a random forest analysis to test the

334   potential for single cell categorisation across all of the groups based on the variance in both charge at

335   t_{50} and effective radius.

336

337   Random forest analysis uses the pre-defined classes (in this case the phytoplankton groupings) to

338   construct a range of 'decision trees' for discrimination of the individual observations (in this case each

339   phytoplankton cell) based upon the predictor variables (in this case charge at t_{50} and effective radius) of

340   a dataset. To effectively test the accuracy of classification, this requires input of a 'training' dataset so

341   that the random forest algorithm can create the necessary discrimination functions for the pre-defined

342   classes. A 'testing' dataset can then be used to determine the accuracy of the discrimination on an

343   independent set of 'blind' observations. As an example of its application in a relevant field, random

344   forest algorithms have previously been used to successfully distinguishing individual populations of

345   phytoplankton strains from flow cytometry measurements on artificial communities (Bestion et al.

346   2020, 2021). Whilst a flow cytometer records a wide range of fluorescence and light scattering variables

347   per individual cell, here we are limited to testing the distinguishing power of our method with only the

348   two aforementioned predictor variables (though additional variables for future iterations of the method

349   are discussed later). Specifically, for our analysis, we used the "randomForest" function in the R

350   package "randomForest"; this function uses Breiman's random forest algorithm for classification

351   (Breiman 2001). From this we could determine categorisation 'decision trees' for two subsets of the

352   susceptibility library data: (a) The key functional groups only (5 groups) with the balanced dataset (see

353   Fig. 3) and (b) all groups (11 groups) with the balanced dataset (see Fig. 5, Table S5). For each subset,

354   we randomly split the datasets using the "*sample_n*" function as described above, assigning 80% of

355   data for the training component, and 20% for the testing. The two input predictor variables of charge at

356   t_{50} and effective radius were natural log transformed prior to running the analysis. Following the training

357 and subsequent testing, confusion matrices were returned to demonstrate the predictions of the random

358 forest models (see Fig. 4 and 6, and Tables S6-S9). At the level of group for each testing subset, we

359 investigated the prediction success in terms of recall, precision, and F1-score metrics (Kraft et al. 2022),

360 see Tables 1 and 2.

361 Recall determines how well the random forest quantifies true positives (TP) for each class *i.e.* a higher

362 recall means fewer false negative predictions are made (FN):

363 Recall = (TP/ (TP + FN))

364 Precision determines how well incorrect false positives (FP) are rejected for each class *i.e.* a higher

365 precision means fewer false positive predictions are made, and more true negatives (TN) are correctly

366 identified:

367 Precision = (TP/(TP+FP))

368 The F1-score combines both the recall and precision into a single metric to define the overall prediction

369 accuracy for each class:

370 F1-score = (2*(precision * recall)/ (precision + recall))

371 In addition to the above, overall accuracy of the random forest was returned to demonstrate the success

372 rate of categorisation across the testing dataset:

373 Accuracy = (TP + TN) / (TP+FP+TN+FN)

374

375
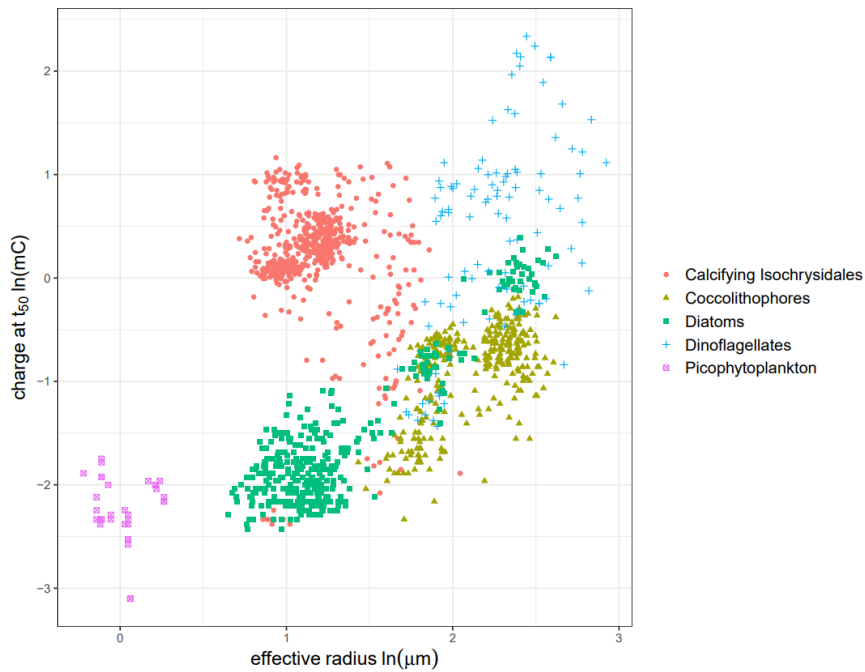
Figure 3. A scatterplot of natural log charge at t_{50} (mC) against natural log effective cell radius (µm) for the 'key functional groups' of cells measured in this study ($n = 1406$, see Table S5 for a summary of the balanced dataset). Whilst there is some overlap of the groupings, the random forest analysis on testing subset of this data returned an overall accuracy of 92% (see Fig. 4, Table 1, and Table S7).
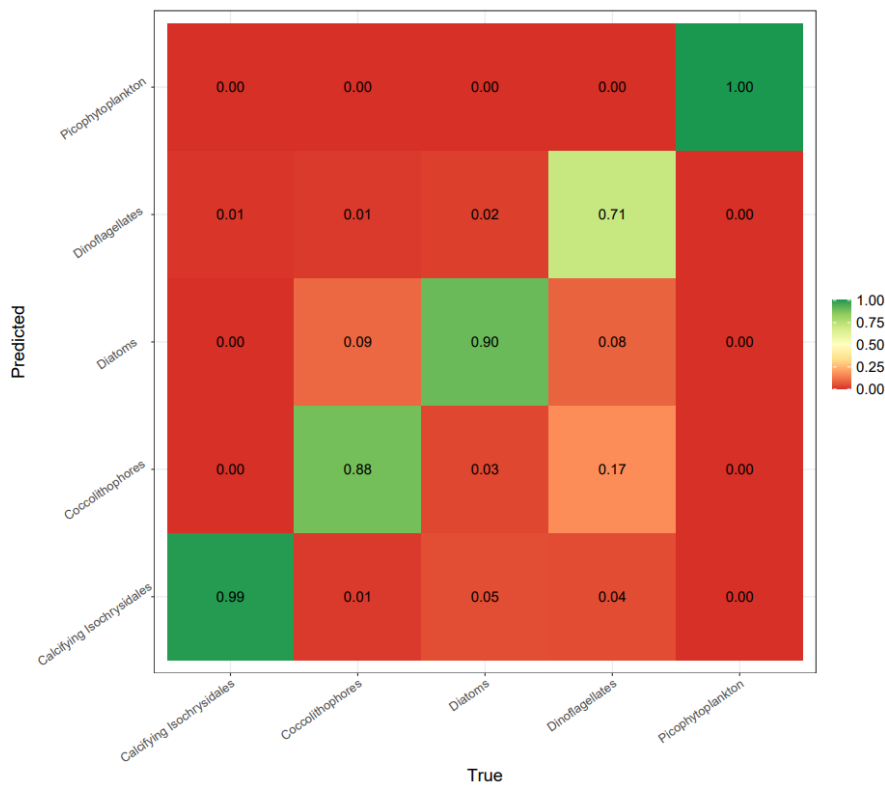
Figure 4. A normalised confusion matrix demonstrating the prediction success of testing the random forest model with just the key groups included. To normalise, predicted number of cases were divided by the true total number of cases in each group (see Table S7 for original values).

13

386 **Table 1.** Evaluation metrics obtained from testing the random forest model trained for the key groups only.

Group	Recall	Precision	F1-score
Calcifying Isochrysidales	0.99	0.95	0.97
Coccolithophores	0.88	0.91	0.89
Diatoms	0.9	0.89	0.9
Dinoflagellates	0.71	0.81	0.76
Picophytoplankton	1	1	1
Overall accuracy			0.92

387

388

389 From training the random forest with the balanced dataset of the key groups only, we found there to be
390 an overall testing accuracy of 92% (see Table 1, and Table S7). The high level of accuracy is perhaps
391 unsurprising considering the visual clustering of the datapoints (see Fig. 3). Within the groupings
392 however, some classifications perform better than others. "Picophytoplankton" are correctly classified
393 in all instances (recall = 1), and this is primarily driven by their much smaller size relative to the other
394 groups. "Calcifying Isochrysidales" are the next best predicted group with a recall of 0.99, and this
395 appears to primarily be driven by their greater electrochemical resilience (*i.e.* greater charge at t_{50})
396 relative to cells of a similar small size. The poorest performance was in classifying "Dinoflagellates",
397 with a recall of 0.71, albeit having a precision score of 0.81. This is likely due to considerable variation
398 in the charge at t_{50} within this group, meaning that some strains of dinoflagellate are misclassified as
399 larger diatoms and coccolithophore, contributing to a greater number of false negatives in this instance.
400 On the whole, the fact that all five of the key groups had F1-scores >0.75 is an indication that the
401 electrochemical sensitivity provides a good degree of separation, in combination with size. Nonetheless,
402 in order to be more reflective of the diversity of nanophytoplankton found in naturally occurring
403 communities, we next considered the level of performance once all of the other groups are included in
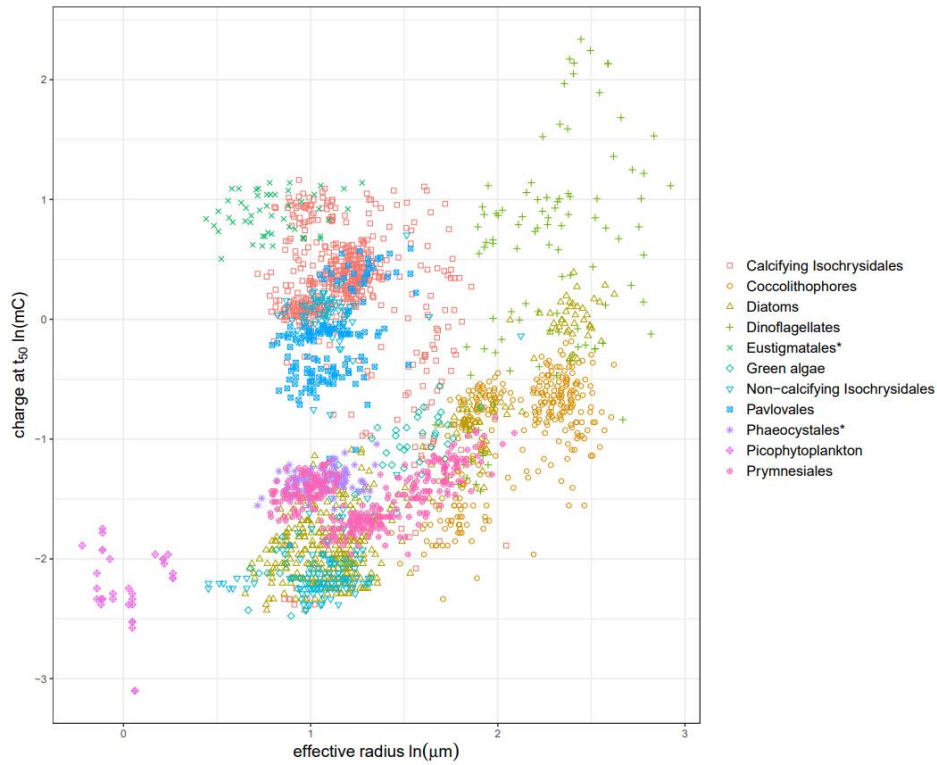404 the random forest analysis (see Fig. 5).

405

406

Figure 5. A scatterplot of natural log charge at t_{50} (mC) against natural log effective cell radius (µm) for all groups
of cells measured in this study (n = 2277, see Table S5 for a summary of the data presented here). Compared to
Fig. 3, where just the key functional groups are presented, we now see more overlap of the groupings. The random
forest analysis on the testing subset of this data returned an overall accuracy of 71% (see Fig. 6, Table 2, and
Table S9). *denotes groups that were just represented by a single species.

412
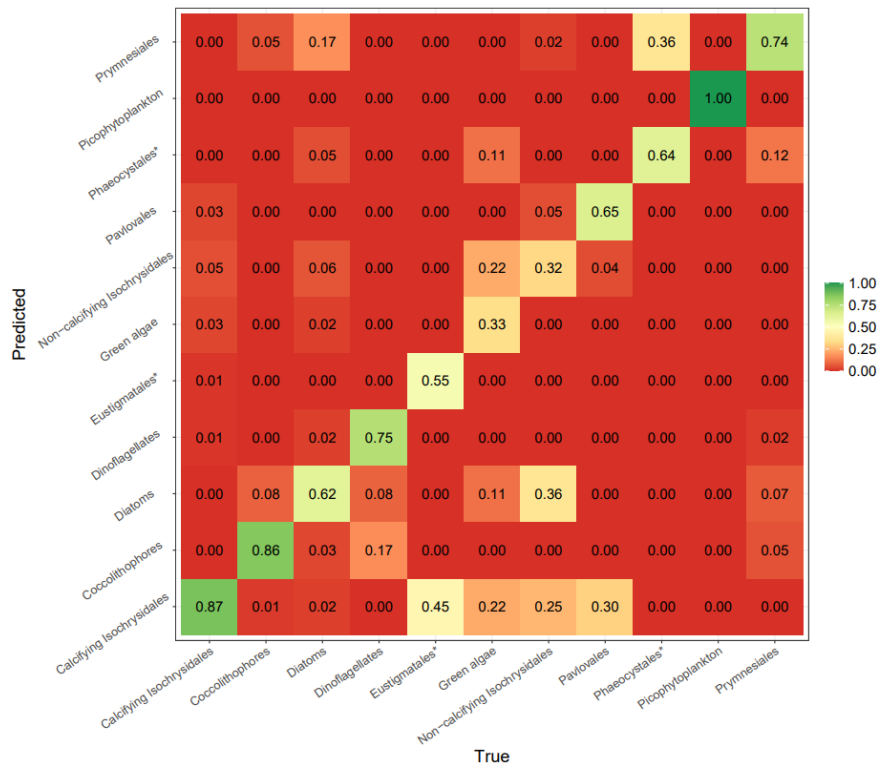
Figure 6. A normalised confusion matrix demonstrating the prediction success of testing the random forest model
with all groups included. To normalise, predicted number of cases were divided by the true total number of cases
in each group (see Table S9 for original values). *denotes groups that were just represented by a single species.

15

Table 2. Evaluation metrics obtained from testing the random forest model trained for all groups. *denotes groups that were just represented by a single species.

Group	Recall	Precision	F1-score
Calcifying Isochrysidales	0.87	0.8	0.83
Coccolithophores	0.86	0.87	0.86
Diatoms	0.63	0.65	0.64
Dinoflagellates	0.75	0.82	0.78
Eustigmatales*	0.55	0.86	0.67
Green algae	0.33	0.33	0.33
Non-calcifying Isochrysidales	0.32	0.5	0.39
Pavlovales	0.65	0.71	0.68
Phaeocystales*	0.64	0.54	0.58
Picophytoplankton	1	1	1
Prymnesiales	0.74	0.61	0.67
Overall accuracy			0.71

When all of the groupings are considered, following training, the overall accuracy on testing was 71% (see Table 2). The lower level of accuracy compared to the interpretation with only the key groups is also unsurprising, given that the number of potential classes in the random forest has more than doubled (5 to 11) and considering the greater extent of overlap in the group level clustering of the datapoints (see Fig. 5). Despite the overall reduction in accuracy, all of the key groups maintain a relatively high level of predictability with all five returning recall, precision and F1 scores of more than 0.6. Of the key groups, the biggest reduction in performance is in the "Diatom" group, with recall being reduced from 0.9 in the key groups subset (see Table 1) to 0.63 when all groups are included. An element of confusion in this instance is being caused by cell types belonging to the other groups, such as "Non-calcifying Isochrysidales" and "Prymnesiales", which have similar size and electrochemical susceptibility distributions. Of the additional groups, the best performing were the "Pavlovales" with an F1-score of 0.68, closely followed by "Prymnesiales" and "Eustigmatales", both with F1-scores of 0.67. The worst performing were, "Green algae" and "Non-calcifying Isochrysidales" with F1-scores of 0.33 and 0.39, respectively. In both cases, considerable confusion was coming from "Diatoms" and "Calcifying Isochrysidales", and specifically for "Green algae" there was substantial confusion with "Non-calcifying Isochrysidales". As dinoflagellates are often the group most commonly associated with harmful algal blooms, it is interesting to note that we see a higher precision (0.82) than recall (0.75) for this group. This indicates that whilst the random forest model is better at rejecting false positives, it could be improved in terms of reducing false negatives (i.e. true cases of dinoflagellate that are being missed). From an applicability point of view, this could suggest that as things stand, improvement is needed if such a technique was to be employed to monitor for potentially harmful algae.

Significantly, of the key groups, there were some notable high performers following testing, despite the inclusion of the other groupings: "Calcifying Isochrysidales" with a recall of 0.87, "Coccolithophores"

16

a recall of 0.86, and for "Picophytoplankton" recall remained at 1. In the case of the "Coccolithophores", their relatively strong predictability is likely due to their low electrochemical resilience relative to their large size, in contrast to "Dinoflagellates" of a comparable size which generally have a greater resilience. "Calcifying Isochrysidales" on the other hand are highly distinguishable for their remarkable electrochemical resilience relative to other groups of a similar smaller size. This poses some key questions about the underlying mechanism of this technique for distinguishing cell types across the groups: How much is cell size driving the electrochemical resilience? Are there any contradicting exceptions to any potential size scaling? With this in mind, we next scrutinise the effect of size on the susceptibility factor to see how much this is driving the overall resilience to the oxidative stress across the groups.

Understanding the mechanism: the size scaling of the relationship and size adjusted resilience

Using the balanced dataset of all groupings, we investigated if there was a significant linear relationship between natural log transformed charge at t_{50} and effective radius (see Fig. 7). This was achieved using the '*lme4*' package in R for linear mixed effects modelling, whereby we fitted and compared linear models to the data both with and without the random effect of grouping on both the intercept and slope of the response. Of the two models, the model including the random effect of grouping on both the slope and intercept scored more favourably than the model without (see Table S10, SI), indicating that there was an overall significant positive linear scaling between charge at t_{50} and effective radius ($p <0.001$), but that this scaling was highly variable across the groupings. The overall model returned a slope value of 0.72 (95% CIs: 0.30 – 1.13). Out of the 11 'groups', 7 of them had significant positive within group size dependence, notably "Green algae", "Diatoms", and "Dinoflagellates" had particularly strong scaling of more than 1 (See Fig. S7 and Table S11, SI). There was no significant size scaling within the groups of "Picophytoplankton", and "Eustigmatales", "Phaeocystales"; this is perhaps unsurprising given that the latter two were only represented by one single strain. Notably, the only group that had a significant negative size scaling were the "Calcifying Isochrysidales", -0.48 (95% CIs: -0.66 – -0.31).

469
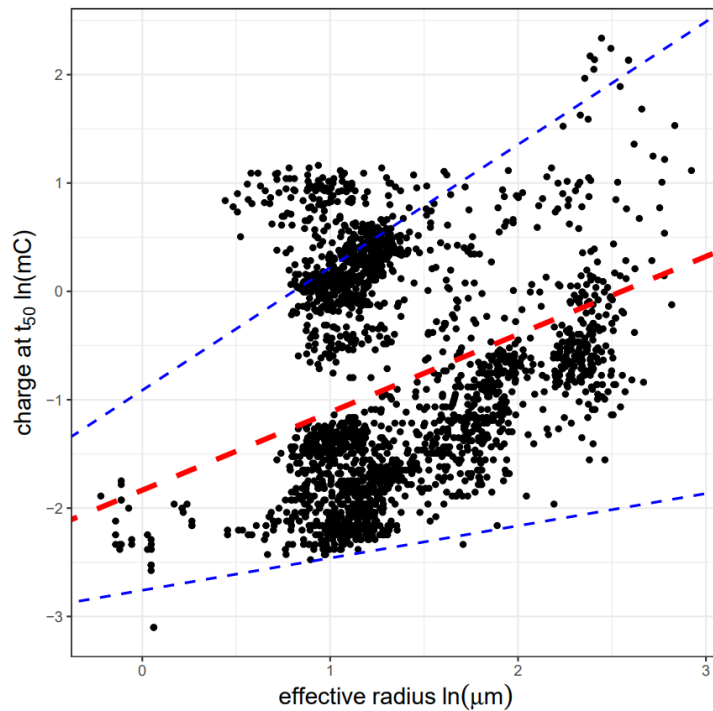
Figure 7. A scatterplot of natural log charge at t_{50} (mC) against natural log effective cell radius (µm) of cells measured in this study, following the balancing of strain representation per group ($n = 2277$, see Table S4 SI for a summary of the data presented here). The red line indicates the overall slope (0.72) of the allometric relationship modelled using linear mixed effects with the random effect of grouping on the slope and intercept factored for, and the blue dashed lines indicate the 95% confidence of this model fit (slopes of 0.30 and 1.13 for lower and upper, respectively), see Tables S10 and S11 for statistics.

On the whole, this demonstrates that across most of the groupings there is an intrinsic allometric scaling of charge required to "switch-off" the chlorophyll *a* signal. This was previously found at the species level in a recent study by Yu *et al*. (2023), which demonstrated that differing electrochemical susceptibility of life stages of *Chlamydomonas concordia*, were primarily driven by size variation in the different cell types, and not necessarily an underlying biological factor (Yu et al. 2023). Consequently, we could postulate that any significant differences in electrochemical susceptibility following a size normalisation might therefore indicate which of the groupings in this study have an 'unknown' underlying biological feature that results in higher or lower resilience. We investigated this by normalising all charge at t_{50} values for size, by simply dividing charge (mC) by effective radius (µm) for each of the individual measurements in the balanced dataset (see Fig. 8).
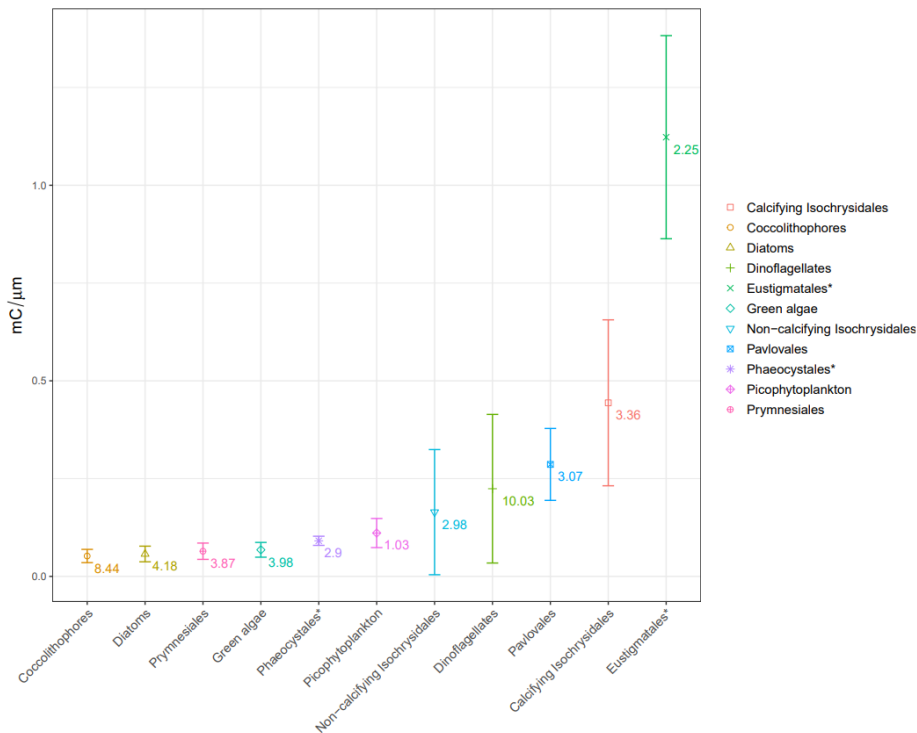
Figure 8. Comparison of per group means of size normalised charge at t_{50}, following the balancing of strain representation per group. Data points represent the mean value for each group and the error bars are for standard deviation. The labelled numbers alongside the data points represent the mean effective radius for each of the groups (in µm), illustrating that in some instances there is a disproportionate resilience to the electrochemical charge relative to cell size – notably for "Calcifying Isochrysidales" and "Eustigmatales". For pairwise comparisons see Table S12, SI. *denotes groups that were just represented by a single species.

Following size normalisation of the charge at t_{50}, we carried out pairwise comparisons across the groups using Pairwise Wilcoxon Rank Sum testing (due to the non-parametric distribution of data in most of the groups), for this we used the function "*pairwise.wilcox.test*" in the R package "*stats*", with "*p.adjust.method*" set to the "Bonferroni" correction of p values see Table S12, SI. We see no significant difference between a number of the key groupings, notably "Diatoms" and "Coccolithophores" ($p = 0.388$), and "Picophytoplankton" and "Dinoflagellates" ($p = 0.325$). Given that "Diatoms" in this dataset have a mean effective radius of 4.18µm (±2.60 S.D.) and "Coccolithophores" of 8.44 µm (±2.20 S.D.), this indicates that most distinguishing between these two groups within the random forest must primarily be driven by size, given that their size normalised charge values are indistinguishable. Likewise, "Picophytoplankton" have a mean effective radius of 1.03 µm (±0.15 S.D.) and "Dinoflagellates" a mean effective radius of 10.03 µm (±3.05 S.D.), demonstrating extreme ends of the size spectrum within this dataset, yet after size normalisation of their respective charge values they are indistinguishable in terms of their electrochemical resilience. Contrary to these observations, it is evident that there are some clear outliers, whereby following size normalisation they are more distinguishable from the rest of the groups, notably "Calcifying Isochrysidales" and "Eustigmatales". In both cases, their size normalised charge was statistically greater than all the other

19

groups, with "Eustigmatales" having the greatest overall per unit size resilience (see Fig. 8, and Table S12). Whilst we only have one strain representing "Eustigmatales" in this dataset, *Nannochloropsis granulata*, we might infer that there is something about the particular biology of these two groups that is driving their greater resistance to the high levels of oxidative stress. This is of relevance to the method, because across all our assessments using the random forest analysis it was the "Calcifying Isochrysidales" group that consistently retained one of the highest levels of prediction accuracy of the key functional groups. Taking our investigation further, we next take a closer look at within species variability to disentangle if any of the particular strains of *E. huxleyi* (from the "Calcifying Isochrysidales" group), representing different life stages and calcification morphologies (Green et al. 1996; Young et al. 2003; Bendif et al. 2023), can help to identify any further trends that may lead to understanding the biological mechanism.
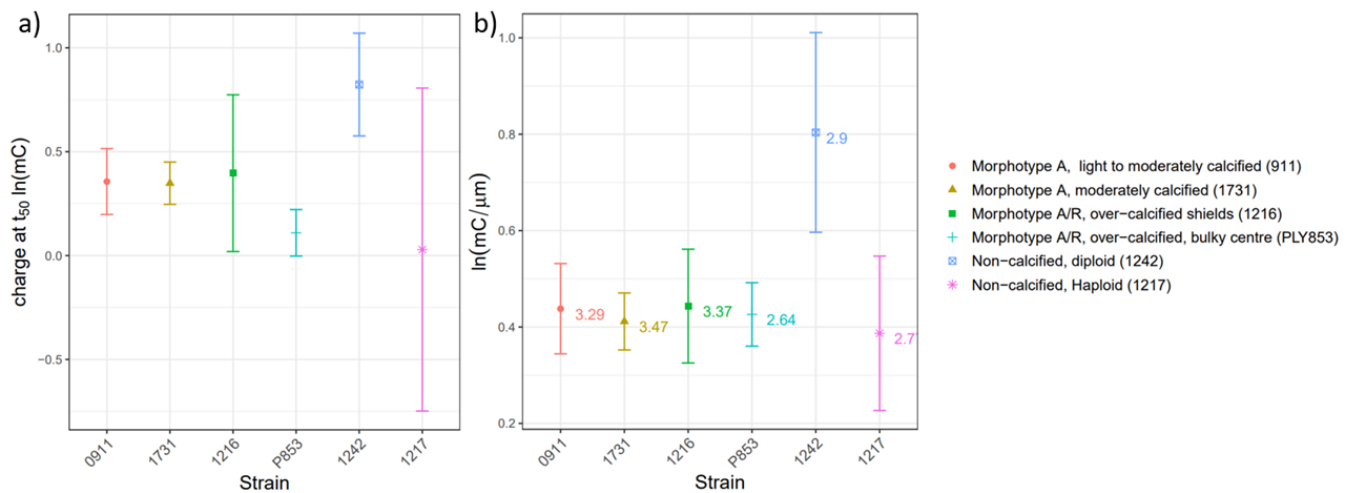
Figure 9. (a) Comparison of natural log transformed mean charge at t_{50} across the different strains of *E. huxleyi* representing different coccosphere morphologies (0911 (RCC911), 1731 (RCC1731), 1216 (RCC1216), (PLY853)), and non-calcified diploid and haploid life stages (1242 (RCC1242), (1217 (RCC1217)). For details on the strains see Table S1, **(b)** Comparison of natural log transformed size normalised charge across the same strains. The labelled numbers alongside the data points represent the mean effective radius for each of the strains (in μm), illustrating that across the strains there is minimal difference in size. For pairwise comparisons see Table S13, SI. For both plots, data points represent the mean value for each group and the error bars are for standard deviation.

Despite their differing coccosphere morphologies (ranging from light-, moderate-, and over- calcified features), in most cases across the four calcified (diploid) strains there was negligible difference in the size normalised charge at t_{50} (see Fig. 9, and Table S13). This result is reassuring in terms of the proposed sensing technology, as it suggests that the within strain variance of "Calcifying Isochrysidales" is not too substantial to cause confusion with other groups. Of particular curiosity, the '1242' non-calcified diploid strain (RCC 1242), had a significantly greater charge per unit size relative to all other strains, and furthermore the '1217' non-calcified haploid strain (RCC 1217) was generally

20

540 indistinguishable from the calcified strains (except for its calcified diploid version RCC 1216). This
541 observation is of relevance to understanding any potential underlying mechanism to the sensor
542 technology for two reasons. Firstly, it indicates that there is minimal effect of the extracellular inorganic
543 calcite layers in either increasing or reducing the resilience of the cell type. This is also more broadly
544 demonstrated when comparing the "Calcifying Isochrysidales" group to the "Coccolithophores", the
545 latter in many instances (*e.g. Coccolithus braarudii*) having much larger extracellular calcium carbonate
546 shell volumes (Yang et al. 2022), yet relatively much faster "switch-off" times and lower size
547 normalised charge tolerance under this method (see Fig. 2b, and Fig. S9, SI). Secondly, it suggests that
548 there is something biologically different between the non-calcified and calcified diploid cells that is
549 driving the discrepancy in the resilience. Disentangling this is beyond the scope of this study, but
550 presents an avenue for further investigation as to why such cell types have greater resilience. Indeed,
551 along a similar vein of thinking, exploring the biological differences of each of the groups against the
552 highly resilient *Nannochloropsis granulata* could help to understand what is driving such resilience
553 irrespective of the cell size. As a tentative suggestion, greater resilience could simply be determined by
554 the membrane structure of the cell, whereby the presence of more membrane layers surrounding the
555 cytoplasm and/or the plastids could potentially present a barrier acting to slow down the transmission
556 of the oxidative radicals to the chlorophyll molecules (Yu et al. 2022). It has previously been reported
557 that *Isochyrsidales* (and specifically *E. huxleyi* and *G. oceani*ca) are distinctive from other
558 coccolithophorids due to a number of different periplast and membrane features, including:
559 unmineralized outer cell scales, more rigid double membrane structures of the peripheral endoplasmic
560 reticulum, and unique long-chain membranous alkenones (Fujiwara et al. 2001). Perhaps it is features,
561 such as these, slowing the transmission of radical oxidants to the chloroplasts of "Calcifying
562 Isochrysidales", resulting in apparent resilience relative to other groups in this study.

563

Discussion

565 Overall our method has demonstrated a good degree of accuracy when it comes to making
566 classifications of cell types into ecologically relevant groups. The groups that consistently had the
567 greatest accuracy were "Calcifying Isochrysidales", "Coccolithophores", and "Picophytoplankton"; all
568 of which maintained a recall of >0.85, and precision and F1-scores of >0.8, across the random forest
569 predictions (both key group and all group libraries). The inclusion of the suspected "nano-
570 phytoflagellate" groups did cause some overall reduction in the accuracy of the technique, from 92% to
571 71%, but given that we have just two variables to make predictions (charge at t_{50} and effective radius),
572 this is something that we anticipate can be improved if the technique was adjusted to capture additional
573 predictor variables. The findings of the susceptibility library assessment also demonstrate that following
574 size normalisation there must be some underlying biological feature that is enhancing the strong
575 classification ability of some of the groups, notably "Calcifying Isochrysidales" and "Eustigmatales",

576 and thus this presents an important avenue for further investigative studies into the potential mechanistic

577 underpinnings.

578

579 **Current applicability of the method and recommendations**

580

581 Whilst we demonstrate the ability of our technique to classify nanophytoplankton into groups of

582 relevance, it is critical that the method can quantify the abundance of different groups in natural

583 seawater samples. This will require field testing alongside more traditional techniques *e.g.* microscope

584 taxonomy and cytometry to validate the applicability of using a predefined susceptibility library based

585 on a limited selection of 52 monocultures. Methodological and engineering advancements will need to

586 be made to take this method to such a stage. As things stand, in obtaining the susceptibility

587 measurements presented here, samples of an uncontrolled volume were drop cast following

588 concentration by centrifugation and left to settle on the electrode beforehand (Kumar et al. 2020).

589 Therefore, given the uncertainties around the volume of sample used, it was not possible to quantify the

590 original abundance of cells in the samples measured. A prototype instrument that implements the fluoro-

591 electrochemical technique with a flow-cell type system could help to overcome this issue, as both

592 sample volume and flow rate could be quantifiable and controllable. To achieve the 'current ramping'

593 approach as demonstrated in this study it is likely that a series of in-flow ring electrodes with different

594 applied currents, separated at periodic intervals, would be required in a future flow-type device. This

595 may allow for a similar level of classification, but with the advantage of the high throughput of a flow-

596 cell setup where number of events can be quantified per unit time, providing a measurement of actual

597 abundance for the different classified cell types. Not only could this make the laboratory-based

598 measurements higher throughput (akin to imaging flow cytometry), it would also be an essential step

599 towards the long-term goal of the technique being used on autonomous platforms, whereby the

600 collection of *in situ* spatio-temporal data of nanophytoplankton community structure would be

601 invaluable to monitoring the effects of environmental change. From a practical point of view, our

602 technique could lend itself well to long-term *in situ* monitoring via an autonomous platform. The

603 electrochemical technique is reagent free (whereby seawater serves as the electrolyte), thus minimising

604 the need for regular retrieval of the device. Furthermore, the production of oxidants on the electrode

605 surface provides an intrinsic anti-fouling mechanism; indeed, electrochemical generation of hydroxyl

606 radicals is a technique that has been successfully used to rapidly kill invasive phytoplankton species in

607 ship's ballast water within seconds, not dissimilar to what we see in the experiments presented here

608 (Zhitao et al. 2005; Bai et al. 2010, 2012; Zhang et al. 2013). Given the relatively simple optics set-up

609 of our technique, compared to others, it is also likely the key components be scaled down from the

610 current lab set-up (see Fig.1a), making it more feasible for deployment in the field.

As mentioned previously, devices such as FlowCam, CytoSense, CytoBuoy and IFCB use combinations of flow cytometry fluorescence measurements with rapid imaging of cells. Whilst highly progressive in helping us to understand planktonic communities, they fall short in their ability to distinguish at the much smaller size ranges – especially when many cell types in the nanophytoplankton range can have a similar apparent morphology and size. Understandably, there is a consequent trade-off between magnification, image quality, and the size range of phytoplankton being measured. This is likely to make any machine learning algorithms poorer at the lower limits of the nanophytoplankton size range. The key novelty of our classifying technique at the nanophytoplankton level is the extra tool for distinguishing phytoplankton cell types that has not been previously applied: the electrochemical susceptibility of the chlorophyll a fluorescence signal, which is less dependent on magnification and image resolution. We can get a good degree of categorisation overall from simply combining the charge at t_{50} value with a simple effective radius estimate. We also demonstrate that our design has potential to distinguish picophytoplankton, as well as larger nanophytoplankton, spanning three orders of magnitude.

It was evident from our assessment that some groups were more easily predicted than others, especially when all the groups were considered. Of the key functional groups, our technique currently falls short when it comes to distinguishing diatoms (F1-score of 0.64, see Table 2), and of the other groups, the lowest accuracy was in predicting "Non-calcifying Isochrysidales" and "Green algae" (F1-scores of 0.39 and 0.33 respectively, see Table 2). Therefore, due to the differing levels of classification ability across the groups as things stand, it is likely the set-up would yield more promising *in situ* measurements from nanophytoplankton communities dominated by taxa belonging to the more easily classifiable groups presented here. To advance our method further, and with minimal increase in cost, a couple of adjustments to both the apparatus and method could give us additional variables that will likely improve predictive ability. Firstly, with the addition of more excitation and emission pathways, a measurement of secondary chlorophyll b pigment fluorescence could be obtained. In marine phytoplankton, this pigment is unique to chlorophytes (or green algae). In the nanophytoplankton range, a large degree of confusion for our method was between the "Diatoms" and "Green algae", and therefore this addition would help to reduce this. Such an advancement could also assist at the picophytoplankton scale, where the majority of pico-eukaryotes are either prasinophytes containing chlorophyll b, or cyanobacteria containing phycocyanin (a chlorophyll accessory pigment, also with distinguishable autofluorescence properties).

Secondly, where there is overlap between calcified cell groups and others, we might be able to use the intrinsic dissolution of the calcite during the electrochemical experiments to observe changes in the apparent radius before and after the experiment. In brief, the electrochemical oxidation of water means that H^+ is generated in the vicinity of the electrode, decreasing the pH around the cells. Consequently, it has been observed that during the short time span of the experimental measurements presented here,

647 the smaller extracellular calcite coccospheres (*e.g. E. huxleyi*) can be completely dissolved, such that a
648 before and after measure of cell radius could indicate the calcification of a cell. Previous work has
649 demonstrated that such a method can also be applied to estimate the mass of extra-cellular calcium
650 carbonate of entire coccospheres (Yang et al. 2022; Fan et al. 2022), which is another relevant
651 measurement for understanding marine biogeochemical cycles, notably the 'rain ratio' (Hutchins 2011).
652 Having an additional predictor variable of the ratio of cellular radius before and after the fluoro-
653 electrochemical experiment would thereby provide an entirely affordable and achievable additional
654 dimension for improved differentiation of calcified and non-calcified cell types in the random forest
655 algorithms, as well as generating an estimate of cellular calcite which could be of great value to ocean
656 biogeochemists.

657 Lastly, additional predictor variables can be gained by taking advantage of the full range of data that is
658 harvested from the experiments presented here. In terms of the chlorophyll *a* fluorescence measurement,
659 we only use a single parameter derived from each transient profile: charge at t_{50}. If the full transient
660 profiles were to be assessed then it is likely this could improve the predictive power of the susceptibility
661 library. Indeed, the shape of the transients appear to be idiosyncratic at a group-specific level (see Fig.
662 S2, SI). With this in mind, by extracting the time (and thus charge) data for additional stages of
663 normalised chlorophyll *a* fluorescence intensity (e.g. at 75%, 25%, 0%) we are more likely to capture
664 the variation in the shape, or gradient, of the 'switch-off' profile. Likewise, in terms of the bright-field
665 imaging, we only make a relatively crude interpretation of the cell radius. There are other variables that
666 can be characterised from the images, such as the minor and major axis lengths to determine aspect
667 ratio (and thus giving an indication on how spherical or elongated a cell is).

668 Taking things forward, whilst we demonstrate relatively good accuracy with just using the two predictor
669 variables used in this study (charge at t_{50} and effective radius), a greater wealth of data could be yielded
670 with only minor methodological tweaks (as suggested above). By training the random forest with more
671 variables (such as: secondary pigment fluorescence, change in cell radius before and after experiment,
672 chlorophyll a fluorescence at different stages in the 'switch-off', and various cell characteristics from
673 2D bright-field images) this is likely to improve the classification accuracy across more of the relevant
674 groups.

675 Overall, following on from the promising results presented here, we foresee that our technique (subject
676 to the improvements discussed) could be extremely complimentary to broader efforts of ocean
677 monitoring. The focus of our technique on the nanophytoplankton size fraction can add detail that is
678 currently missing from existing techniques. As we demonstrate, there is potential for distinguishing
679 cells into relevant groupings, going beyond the limited capacity of standard flow cytometry where, as
680 things stand, only a select few of the functional groups can be differentiated within nanoeukaryotic
681 communities; coccolithophores and cryptophytes (Tarran et al. 2006; Tarran and Bruun 2015).

682 Furthermore, as discussed above, the application of our technique would help to unlock detail at the
683 finer size scale that is also poorly characterised by current *in situ* imaging flow cytometry. Through
684 developing our 'susceptibility library' with a diverse range of taxa, we also expect that our technique
685 could help to tease out more information from previously labelled unknown 'nano-phytoflagellate'
686 populations in natural communities, which are notoriously problematic for taxonomists due to their
687 similar sizes and morphology when viewed under the microscope (Widdicombe et al. 2010; Piwosz
688 2019). For example, both "Pavlovales" and "Prymnesiales" haptophyte groups in this study had F1-
689 scores of >0.65, indicating that whilst they might be of a similar size and morphology (and thus are
690 likely "nano-phytoflagellate" candidates), they are somewhat distinguishable by their susceptibility to
691 the electrochemically driven oxidative conditions.

692

693 **Summary**

694

695 We have presented a novel fluoro-electrochemical technique for classifying marine nanophytoplankton,
696 and critically assessed this by testing its ability to predict phytoplankton groupings from two simple
697 parameters: charge required to reduce per cell chlorophyll *a* fluorescence by 50% and effective cell
698 radius. This returned an excellent degree of accuracy when only considering taxa belonging to key
699 functional groups (5 groups), but a reduced degree of accuracy when a broader range of groups,
700 encompassing likely "nano-phytoflagellates", were considered (11 groups). We demonstrate that the
701 technique relies on the general positive size scaling of the susceptibility across the groups to provide
702 additional distinguishing power, and when size is normalised for there are some groups that demonstrate
703 exceptional resilience to the highly oxidative conditions of our technique, notably "Calcifying
704 Isochrysidales" and "Eustigmatales". This presents an avenue for further investigation into the
705 biological underpinnings of this new method. Whilst the technique currently has its limitations as we
706 report, with advancement of the set-up to make complimentary measurements, the predictive power of
707 the method could be enhanced. Critically, if the technique is to eventually be used for real world *in situ*
708 measurements, the next step of assessment is to test its ability in quantifying abundance of different
709 groupings in natural samples alongside more traditional techniques. If such further testing yields
710 positive results, we anticipate that our technique could be adapted to work in conjunction with
711 autonomous platforms, with the potential to greatly enhance our ability in monitoring
712 nanophytoplankton community structure.

713

714

715

References

Álvarez, E., M. Moyano, Á. López-Urrutia, E. Nogueira, and R. Scharek. 2014. Routine determination of plankton community composition and size structure: A comparison between FlowCAM and light microscopy. J Plankton Res **36**: 170–184. doi:10.1093/plankt/fbt069

Alves-De-Souza, C., T. S. Benevides, J. B. O. Santos, P. Von Dassow, L. Guillou, and M. Menezes. 2017. Does environmental heterogeneity explain temporal β diversity of small eukaryotic phytoplankton? Example from a tropical eutrophic coastal lagoon. J Plankton Res **39**: 698–714. doi:10.1093/plankt/fbx026

Anderson, S. I., A. D. Barton, S. Clayton, S. Dutkiewicz, and T. A. Rynearson. 2021. Marine phytoplankton functional types exhibit diverse responses to thermal change. Nat Commun **12**. doi:10.1038/s41467-021-26651-8

Anderson, T. R. 2005. Plankton functional type modelling: Running before we can walk? J Plankton Res **27**: 1073–1081. doi:10.1093/plankt/fbi076

Bai, M., Z. Zhang, X. Xue, X. Yang, L. Hua, and D. Fan. 2010. Killing Effects of Hydroxyl Radical on Algae and Bacteria in Ship's Ballast Water and on Their Cell Morphology. Plasma Chemistry and Plasma Processing **30**: 831–840. doi:10.1007/s11090-010-9252-5

Bai, M., Z. Zhang, N. Zhang, Y. Tian, C. Chen, and X. Meng. 2012. Treatment of 250 t/h Ballast Water in Oceanic Ships Using ·OH Radicals Based on Strong Electric-Field Discharge. Plasma Chemistry and Plasma Processing **32**: 693–702. doi:10.1007/s11090-012-9369-9

Balzano, S., D. Marie, P. Gourvil, and D. Vaulot. 2012. Composition of the summer photosynthetic pico and nanoplankton communities in the Beaufort Sea assessed by T-RFLP and sequences of the 18S rRNA gene from flow cytometry sorted samples. ISME Journal **6**: 1480–1498. doi:10.1038/ismej.2011.213

Barnes, M. K., G. H. Tilstone, D. J. Suggett, C. E. Widdicombe, J. Bruun, V. Martinez-Vicente, and T. J. Smyth. 2015. Temporal variability in total, micro- and nano-phytoplankton primary production at a coastal site in the Western English Channel. Prog Oceanogr **137**: 470–483. doi:10.1016/j.pocean.2015.04.017

Bendif, E. M., I. Probert, O. A. Archontikis, J. R. Young, L. Beaufort, R. E. Rickaby, and D. Filatov. 2023. Rapid diversification underlying the global dominance of a cosmopolitan phytoplankton. ISME J. doi:10.1038/s41396-023-01365-5

755 Bestion, E., S. Barton, F. C. García, R. Warfield, and G. Yvon-Durocher. 2020. Abrupt declines in
756   marine phytoplankton production driven by warming and biodiversity loss in a microcosm
757   experiment. Ecol Lett **23**: 457–466. doi:10.1111/ele.13444

758 Bestion, E., B. Haegeman, S. Alvarez Codesal, A. Garreau, M. Huet, S. Barton, and J. M. Montoya.
759   2021. Phytoplankton biodiversity is more important for ecosystem functioning in highly variable
760   thermal environments. PNAS **118**. doi:10.1073/pnas.2019591118

761 Bolaños, L. M., L. Karp-Boss, C. J. Choi, and others. 2020. Small phytoplankton dominate western
762   North Atlantic biomass. ISME Journal **14**: 1663–1674. doi:10.1038/s41396-020-0636-0

763 Breiman, L. 2001. Random Forests. Mach Learn **45**: 5–32. doi:10.1023/A:1010933404324

764 Camoying, M. G., and A. T. Yñiguez. 2016. FlowCAM optimization: Attaining good quality images
765   for higher taxonomic classification resolution of natural phytoplankton samples. Limnol
766   Oceanogr Methods **14**: 305–314. doi:10.1002/lom3.10090

767 Chase, A. P., S. J. Kramer, N. Haëntjens, E. S. Boss, L. Karp-Boss, M. Edmondson, and J. R. Graff.
768   2020. Evaluation of diagnostic pigments to estimate phytoplankton size classes. Limnol
769   Oceanogr Methods **18**: 570–584. doi:10.1002/lom3.10385

770 Collier, J. L. 2000. Flow cytometry and the single cell in phycology. J Phycol **36**: 628–644.
771   doi:10.1046/j.1529-8817.2000.99215.x

772 Dubelaar, G. B. J., P. L. Gerritzen, A. E. R. Beeker, R. R. Jonker, and K. Tangen. 1999. Design and
773   first results of CytoBuoy: A wireless flow cytometer for in situ analysis of marine and fresh
774   waters. Cytometry **37**: 247–254. doi:10.1002/(SICI)1097-0320(19991201)37:4<247::AID-
775   CYTO1>3.0.CO;2-9

776 Dugenne, M., M. Thyssen, D. Nerini, C. Mante, J. C. Poggiale, N. Garcia, F. Garcia, and G. J.
777   Grégori. 2014. Consequence of a sudden wind event on the dynamics of a coastal phytoplankton
778   community: An insight into specific population growth rates using a single cell high frequency
779   approach. Front Microbiol **5**. doi:10.3389/fmicb.2014.00485

780 Fan, X., C. Batchelor-McAuley, M. Yang, S. Barton, R. E. M. Rickaby, H. A. Bouman, and R. G.
781   Compton. 2022. Quantifying the Extent of Calcification of a Coccolithophore Using a Coulter
782   Counter. Anal Chem **94**: 12664–12672. doi:10.1021/acs.analchem.2c01971

783 Finkel, Z. V., J. Beardall, K. J. Flynn, A. Quigg, T. A. V. Rees, and J. A. Raven. 2010. Phytoplankton
784   in a changing world: Cell size and elemental stoichiometry. J Plankton Res **32**: 119–137.
785   doi:10.1093/plankt/fbp098

786 Fragoso, G. M., A. J. Poulton, N. J. Pratt, G. Johnsen, and D. A. Purdie. 2019. Trait-based analysis of
787   subpolar North Atlantic phytoplankton and plastidic ciliate communities using automated flow
788   cytometer. Limnol Oceanogr **64**: 1763–1778. doi:10.1002/lno.11189

789 Fuchs, R., M. Thyssen, V. Creach, and others. 2022. Automatic recognition of flow cytometric
790   phytoplankton functional groups using convolutional neural networks. Limnol Oceanogr
791   Methods **20**: 387–399. doi:10.1002/lom3.10493

792 Fujiwara, S., M. Tsuzuki, M. Kawachi, and N. Minaka. 2001. MOLECULAR PHYLOGENY OF
793   THE HAPTOPHYTA BASED ON THE rbc L GENE AND SEQUENCE VARIATION IN THE
794   SPACER REGION OF THE RUBISCO OPERON 1. J Phycol **37**: 121–129.

795 Green, J., P. Course, and G. Tarran. 1996. The life-cycle of Emiliania huxleyi: A brief review and a
796   study of relative ploidy levels analysed by flow cytometry. Journal of Marine Systems **9**: 33–44.

797 Haraguchi, L., H. Jakobsen, N. Lundholm, and J. Carstensen. 2017. Monitoring natural phytoplankton
798   communities: a comparison between traditional methods and pulse-shape recording flow
799   cytometry. Aquatic Microbial Ecology **80**: 77–92. doi:10.3354/ame01842

800 Hutchins, D. A. ,. 2011. Forecasting the rain ratio. Nature **476**: 41–42.

801 Irisson, J.-O., S.-D. Ayata, D. J. Lindsay, L. Karp-Boss, and L. Stemmann. 2022. Machine Learning
802   for the Study of Plankton and Marine Snow from Images. Ann Rev Mar Sci **14**: 277–301.
803   doi:10.1146/annurev-marine-041921

804 Kraft, K., J. Seppälä, H. Hällfors, and others. 2021. First Application of IFCB High-Frequency
805   Imaging-in-Flow Cytometry to Investigate Bloom-Forming Filamentous Cyanobacteria in the
806   Baltic Sea. Front Mar Sci **8**. doi:10.3389/fmars.2021.594144

807 Kraft, K., O. Velhonoja, T. Eerola, and others. 2022. Towards operational phytoplankton recognition
808   with automated high-throughput imaging, near-real-time data processing, and convolutional
809   neural networks. Front Mar Sci **9**. doi:10.3389/fmars.2022.867695

810 Kumar, A. K. S., Y. Zhang, D. Li, and R. G. Compton. 2020. A mini-review: How reliable is the drop
811   casting technique? Electrochem commun **121**. doi:10.1016/j.elecom.2020.106867

812 Leblanc, K., B. Quéguiner, F. Diaz, and others. 2018. Nanoplanktonic diatoms are globally
813   overlooked but play a role in spring blooms and carbon export. Nat Commun **9**.
814   doi:10.1038/s41467-018-03376-9

815 Litchman, E., and C. A. Klausmeier. 2008. Trait-based community ecology of phytoplankton. Annu
816   Rev Ecol Evol Syst **39**: 615–639. doi:10.1146/annurev.ecolsys.39.110707.173549

817 Lombard, F., E. Boss, A. M. Waite, and others. 2019. Globally consistent quantitative observations of
818   planktonic ecosystems. Front Mar Sci **6**. doi:10.3389/fmars.2019.00196

819 López-Sandoval, D. C., T. Rodríguez-Ramos, P. Cermeño, C. Sobrino, and E. Marañón. 2014.
820   Photosynthesis and respiration in marine phytoplankton: Relationship with cell size, taxonomic
821   affiliation, and growth phase. J Exp Mar Biol Ecol **457**: 151–159.
822   doi:10.1016/j.jembe.2014.04.013

823 Marañón, E., P. Cermeño, D. C. López-Sandoval, T. Rodríguez-Ramos, C. Sobrino, M. Huete-Ortega,
824   J. M. Blanco, and J. Rodríguez. 2013. Unimodal size scaling of phytoplankton growth and the
825   size dependence of nutrient uptake and use. Ecol Lett **16**: 371–379. doi:10.1111/ele.12052

826 Morel, F. M. M., J. G. Rueter, D. M. Anderson, and R. R. L. Guillard. 1979. AQUIL: A
827   CHEMICALLY DEFINED PHYTOPLANKTON CULTURE MEDIUM FOR TRACE METAL
828   STUDIES 1 2 . J Phycol **15**: 135–141. doi:10.1111/j.1529-8817.1979.tb02976.x

829 Nair, A., S. Sathyendranath, T. Platt, J. Morales, V. Stuart, M. H. Forget, E. Devred, and H. Bouman.
830   2008. Remote sensing of phytoplankton functional types. Remote Sens Environ **112**: 3366–
831   3375. doi:10.1016/j.rse.2008.01.021

832 Olson, R. J., and H. M. Sosik. 2007. A submersible imaging-in-flow instrument to analyze nano-and
833   microplankton: Imaging FlowCytobot. Limnol Oceanogr Methods **5**: 195–203.
834   doi:10.4319/lom.2007.5.195

835 Pinckney, J. L., C. R. Benitez-Nelson, R. C. Thunell, F. Muller-Karger, L. Lorenzoni, L. Troccoli, and
836   R. Varela. 2015. Phytoplankton community structure and depth distribution changes in the
837   Cariaco Basin between 1996 and 2010. Deep Sea Res 1 Oceanogr Res Pap **101**: 27–37.
838   doi:10.1016/j.dsr.2015.03.004

839   Piwosz, K. 2019. Weekly dynamics of abundance and size structure of specific nanophytoplankton
840   lineages in coastal waters (Baltic Sea). Limnol Oceanogr **64**: 2172–2186. doi:10.1002/lno.11177

841   Sieracki, C. K., M. E. Sieracki, and C. S. Yentsch. 1998. An imaging-in-flow system for automated
842   analysis of marine microplankton. Mar Ecol Prog Ser **168**: 285–296.

843   Snoeijs, P., S. Busse, and M. Potapova. 2002. The importance of diatom cell size in community
844   analysis. J Phycol **38**: 265–281. doi:10.1046/j.1529-8817.2002.01105.x

845   Sosik, H. M., and R. J. Olson. 2007. Automated taxonomic classification of phytoplankton sampled
846   with imaging-in-flow cytometry. Limnol Oceanogr Methods **5**: 204–216.
847   doi:10.4319/lom.2007.5.204

848   Stern, R., K. Picard, J. Clarke, and others. 2023. Composition and Patterns of Taxa Assemblages in
849   the Western Channel Assessed by 18S Sequencing, Microscopy and Flow Cytometry. J Mar Sci
850   Eng **11**: 480. doi:10.3390/jmse11030480

851   Tarran, G. A., and J. T. Bruun. 2015. Nanoplankton and picoplankton in the Western English
852   Channel: Abundance and seasonality from 2007-2013. Prog Oceanogr **137**: 446–455.
853   doi:10.1016/j.pocean.2015.04.024

854   Tarran, G. A., J. L. Heywood, and M. V. Zubkov. 2006. Latitudinal changes in the standing stocks of
855   nano- and picoeukaryotic phytoplankton in the Atlantic Ocean. Deep Sea Res 2 Top Stud
856   Oceanogr **53**: 1516–1529. doi:10.1016/j.dsr2.2006.05.004

857   de Vargas, C., S. Audic, N. Henry, and others. 2015. Eukaryotic plankton diversity in the sunlit ocean.
858   Science (1979) **348**. doi:10.1126/science.1261605

859   Ward, B. A., E. Marañón, B. Sauterey, J. Rault, and D. Claessen. 2017. The size dependence of
860   phytoplankton growth rates: A trade-off between nutrient uptake and metabolism. American
861   Naturalist **189**: 170–177. doi:10.1086/689992

862   Widdicombe, C. E., D. Eloire, D. Harbour, R. P. Harris, and P. J. Somerfield. 2010. Long-term
863   phytoplankton community dynamics in the Western English Channel. J Plankton Res **32**: 643–
864   655. doi:10.1093/plankt/fbp127

865   Yang, M., C. Batchelor-McAuley, S. Barton, R. E. M. Rickaby, H. A. Bouman, and R. G. Compton.
866   2022. Single-entity coccolithophore electrochemistry shows size is no guide to the degree of
867   calcification. Environmental Science: Advances **1**: 156–163. doi:10.1039/d2va00025c

868   Yang, M., C. Batchelor-Mcauley, L. Chen, Y. Guo, Q. Zhang, R. E. M. Rickaby, H. A. Bouman, and
869   R. G. Compton. 2019. Fluoro-electrochemical microscopy reveals group specific differential
870   susceptibility of phytoplankton towards oxidative damage. Chem Sci **10**: 7988–7993.
871   doi:10.1039/c9sc02699a

872   Young, J., M. Geisen, L. Cros, A. Kleijne, C. Sprengel, I. Probert, and J. Østergaard. 2003. A guide to
873   extant coccolithophore taxonomy. Journal of Nannoplankton Research, Special Issue **1**: 1–132.

874   Yu, J., M. Yang, C. Batchelor-McAuley, S. Barton, R. E. M. Rickaby, H. A. Bouman, and R. G.
875   Compton. 2022. Rapid Opto-electrochemical Differentiation of Marine Phytoplankton. ACS
876   Measurement Science Au **2**: 342–350. doi:10.1021/acsmeasuresciau.2c00017

877   Yu, J., M. Yang, C. Batchelor-McAuley, S. Barton, R. E. M. Rickaby, H. A. Bouman, and R. G.
878   Compton. 2023. Does the life cycle stage matter for distinguishing phytoplankton via fluoro-
879   electrochemical microscopy? Cell Rep Phys Sci **4**. doi:10.1016/j.xcrp.2022.101223

880   Zhang, Y., M. Bai, C. Chen, X. Meng, Y. Tian, N. Zhang, and Z. Yu. 2013. ·OH Treatment for
881   Killing of Harmful Organisms in Ship's Ballast Water with Medium Salinity Based on Strong
882   Ionization Discharge. Plasma Chemistry and Plasma Processing **33**: 751–763.
883   doi:10.1007/s11090-013-9464-6

884   Zhitao, Z., B. Mindong, Y. Bo, B. Mindi, and B. Xiyao. 2005. Treatment of Invasive Marine Species
885   on Board by Using Micro-gap Discharge Plasma. Plasma Science and Technology **7**: 3025–
886   3029. doi:10.1088/1009-0630/7/5/011

887

888

889 **Supplemental Information for:**

890 **A novel fluoro-electrochemical technique for classifying diverse marine**
891 **nanophytoplankton**

892

893 Samuel Barton[1*], Minjun Yang[2], Haotian Chen[2], Christopher Batchelor-McAuley[2, 3], Richard
894 G. Compton[2], Heather A. Bouman[1], Rosalind E.M. Rickaby[1]

895

896 [1] Department of Earth Sciences, University of Oxford, South Parks Road, Oxford, OX1 3AN, UK

897 [2] Physical and Theoretical Chemistry Laboratory, Department of Chemistry, University of Oxford,
898 South Parks Road, Oxford, OX1 3QZ, UK

899 [3] School of Chemistry, Trinity College Dublin, Dublin 2, Ireland

900 * Corresponding author: samuel.barton@earth.ox.ac.uk

901

902 Number of Figures: 9 (pages 2 - 8)

903 Number of Tables: 13 (pages 9 – 19)

904 References: 4 (page 20)

905

906

907
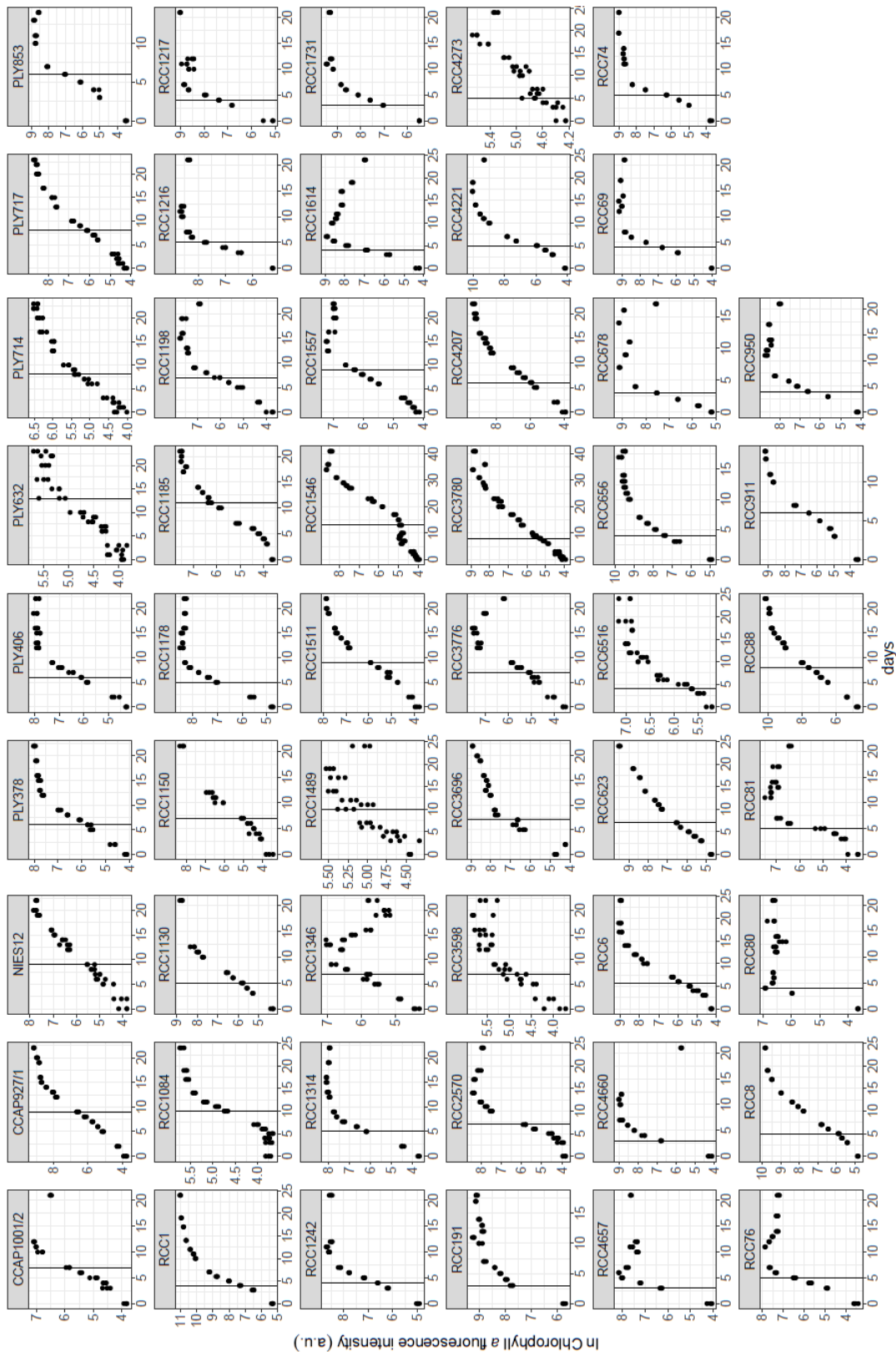
Figure S1: Culture growth curves for each of the strains listed in Table S1, as natural log transformed Chlorophyll *a* fluorescence intensity against days. The data points represent technical replicated measurements for each culture on each day. The vertical black line corresponds to the time-point when the electrochemical measurements were made, as described in the main text.

912

913
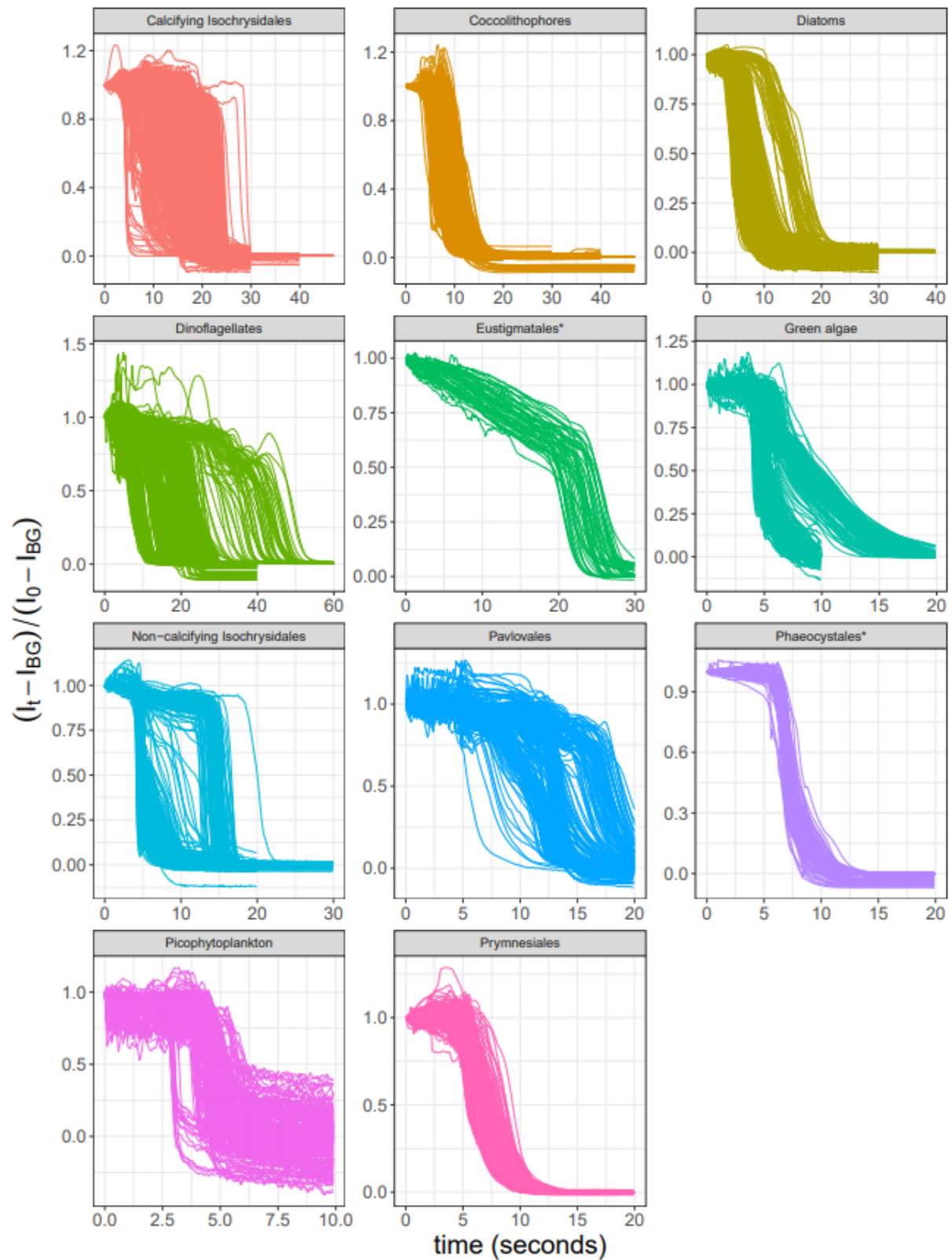
Figure S2: Normalised Chlorophyll *a* fluorescence transients for each of the relevant phytoplankton groups in this study. Each line represents a single cell measurement (4884 individual cell measurements in total, across the groups). Time '0 seconds' is the time-point when the current ramping of the electrochemical experiments commenced. *denotes groups that were just represented by a single species.

919

920
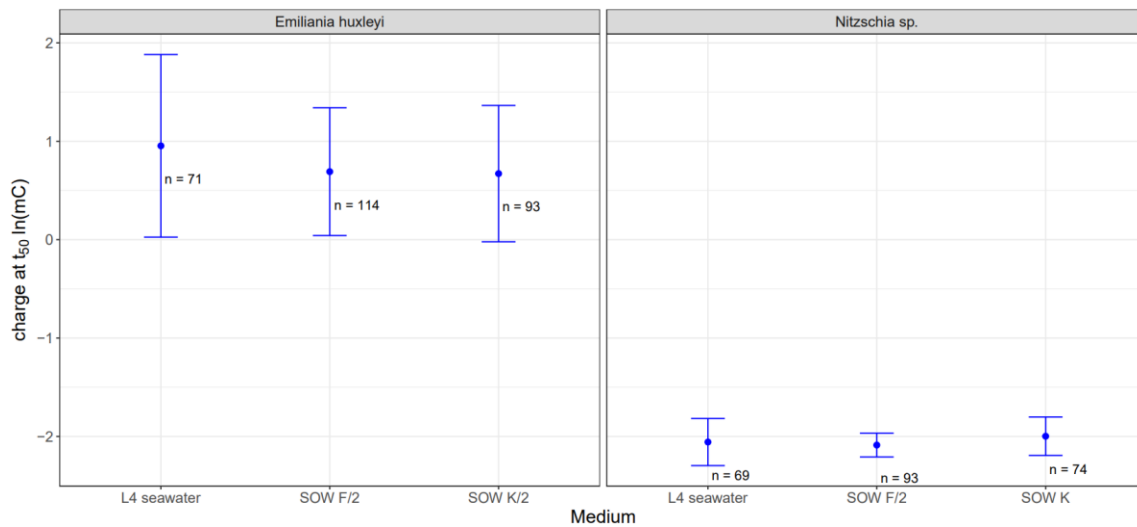
Figure S3: Mean and standard deviation of natural log charge at t_{50} (in mC) measured for each of the strains when using different mediums as electrolyte. In the case of the calcifying isochrysidale *Emiliania huxleyi* (RCC1216), SOW K/2 (synthetic ocean water enriched with K/2 medium stocks) was the original growth medium. For the diatom *Nitzschia* sp. (RCC80), SOW K (synthetic ocean water enriched with K medium stocks) was the original growth medium. For each of the above, 15mL of culture in exponential growth phase was centrifuged at 1000 r.p.m for 10 minutes, supernatant (original growth medium) was removed, and pelleted cells were resuspended in either L4 seawater or SOW F/2 (synthetic ocean water enriched with F/2 medium stocks). L4 seawater is natural seawater (collected at 10m depth from the L4 station, Western Channel Observatory, English Channel), which had been aged and refrigerated in the dark for > 1 year and 0.22µm filtered prior to making measurements. Numbers alongside data points represent the number of cells measured with each medium. Considering the deviation in the values, there is a negligible effect of each medium (or electrolyte) on the susceptibility of the strains. It is also clear that the variance for each medium response is within the broader range of values obtained for the strains' respective classified groups in the 'susceptibility library (see Fig. 3 and Fig. S5).

936

937

938
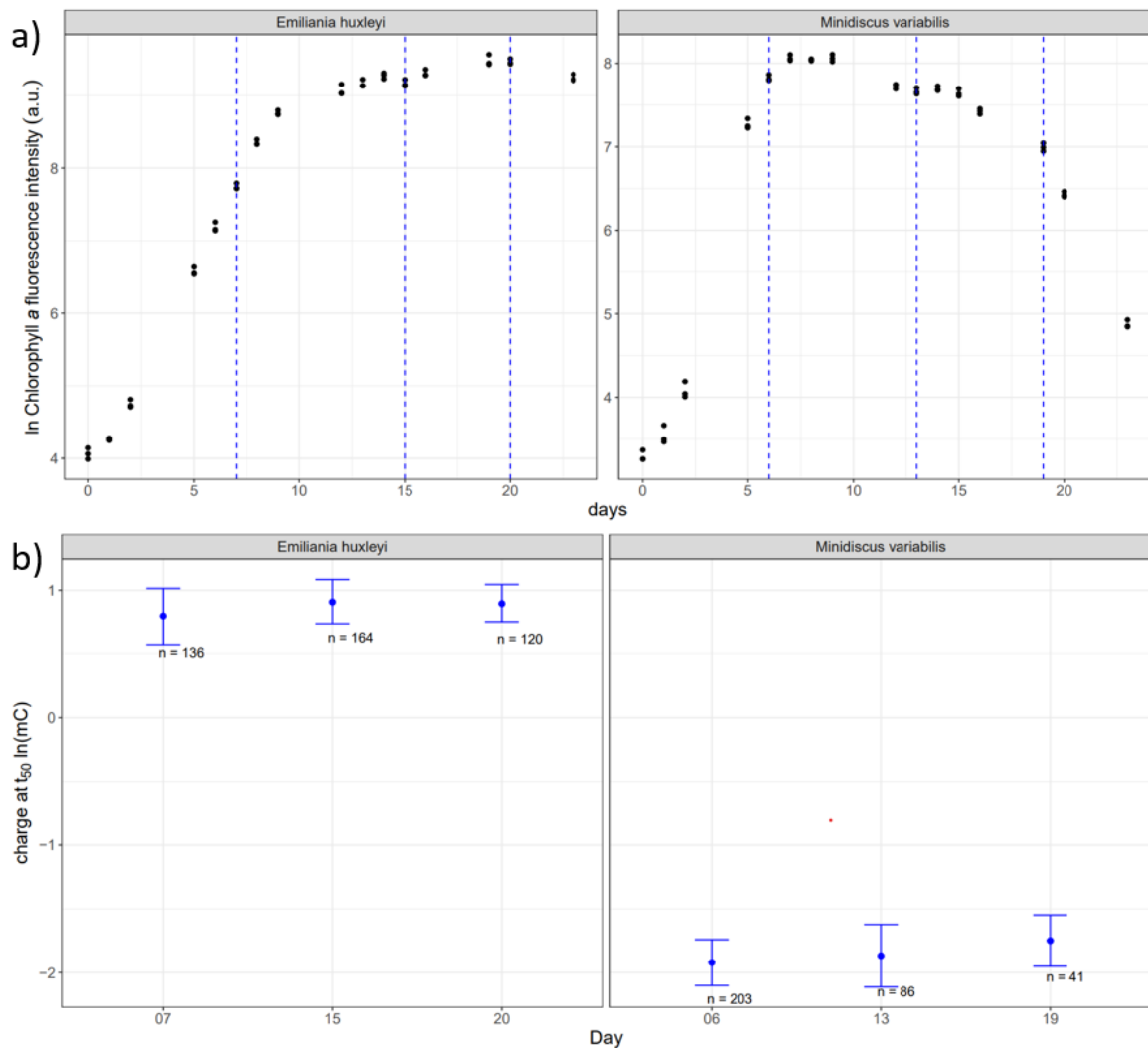
Figure S4: (a) Culture growth curves for two strains: the calcifying isochryisdale *Emiliania huxleyi* (RCC 1731) and the diatom *Minidiscus variabilis* (RCC 4657), as natural log transformed Chlorophyll *a* fluorescence intensity against days. The data points represent technical replicated measurements for each culture on each day. The vertical dashed blue lines correspond to the time-points when the electrochemical measurements were made **(b)** Mean and standard deviation of natural log charge at t_{50} (in mC) measured for each of the strains, at each of the labelled time-points in (a). Numbers alongside data points represent the number of cells measured. As can be seen, there is a negligible effect of population growth stage on the susceptibility of the strains. Furthermore, it is clear that the variance of data from each point of the growth curve is within the range of values obtained for the strains' respective classified groups in the 'susceptibility library', where all measurements were made in the exponential growth phase (see Fig. 3 and Fig. S5).

950

951

952

953
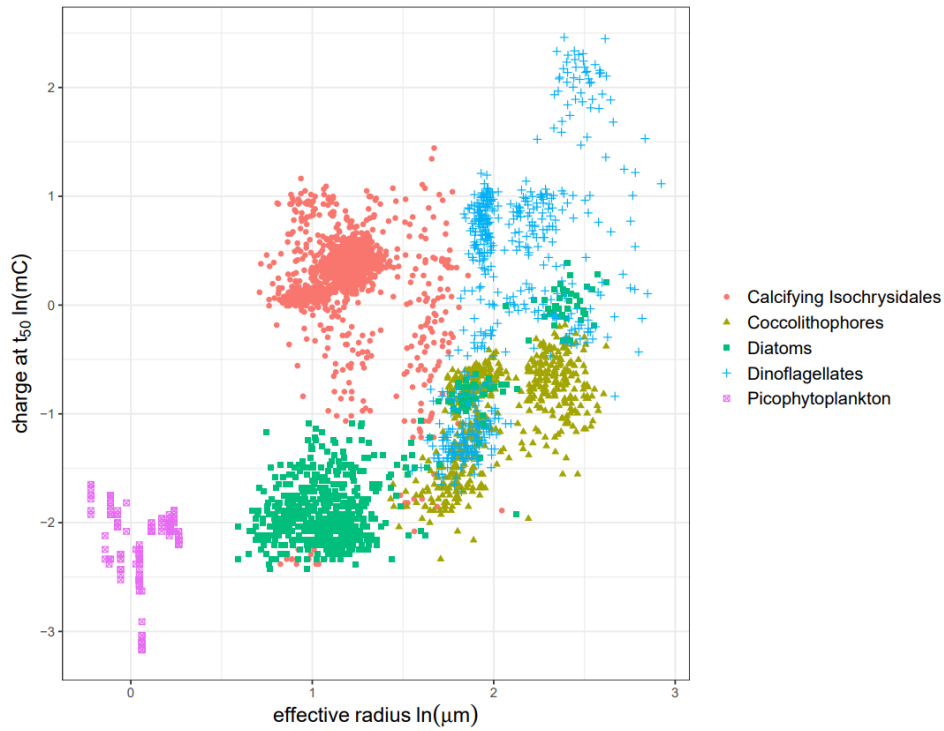
Figure S5: A scatterplot of natural log charge at t_{50} (mC) against natural log effective cell radius (µm) for the 'key functional groups' of cells measured in this study, using the unbalanced dataset ($n = 3880$).

956
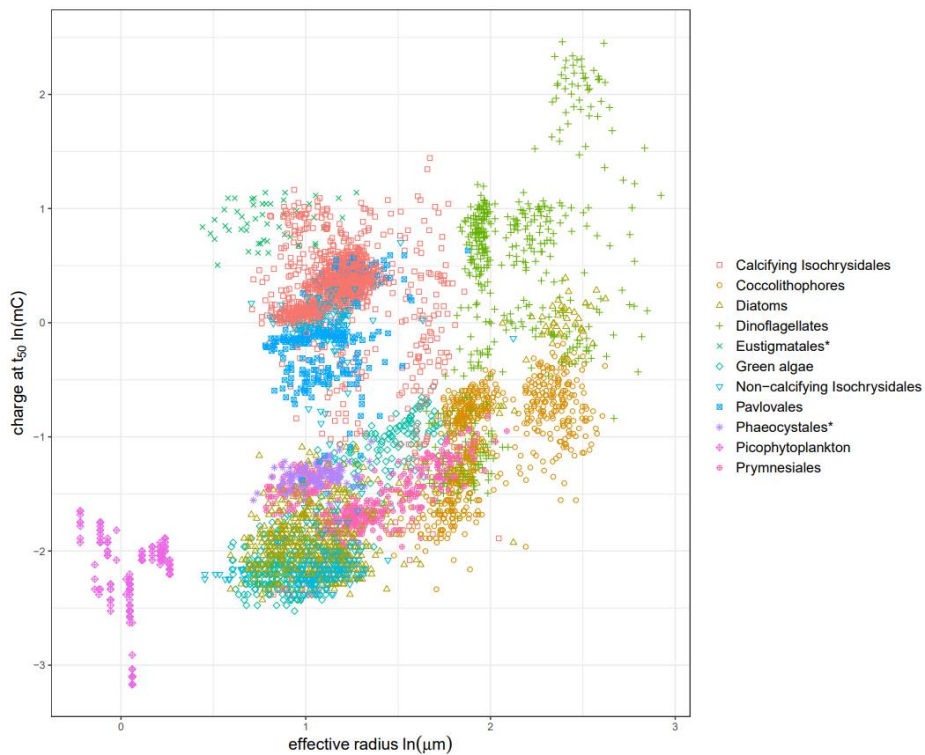
Figure S6: A scatterplot of natural log charge at t_{50} (mC) against natural log effective cell radius (µm) for all groups of cells measured in this study, with the unbalanced dataset ($n = 4884$, see Table S3 for a summary of the data presented here). *denotes groups that were just represented by a single species.

960
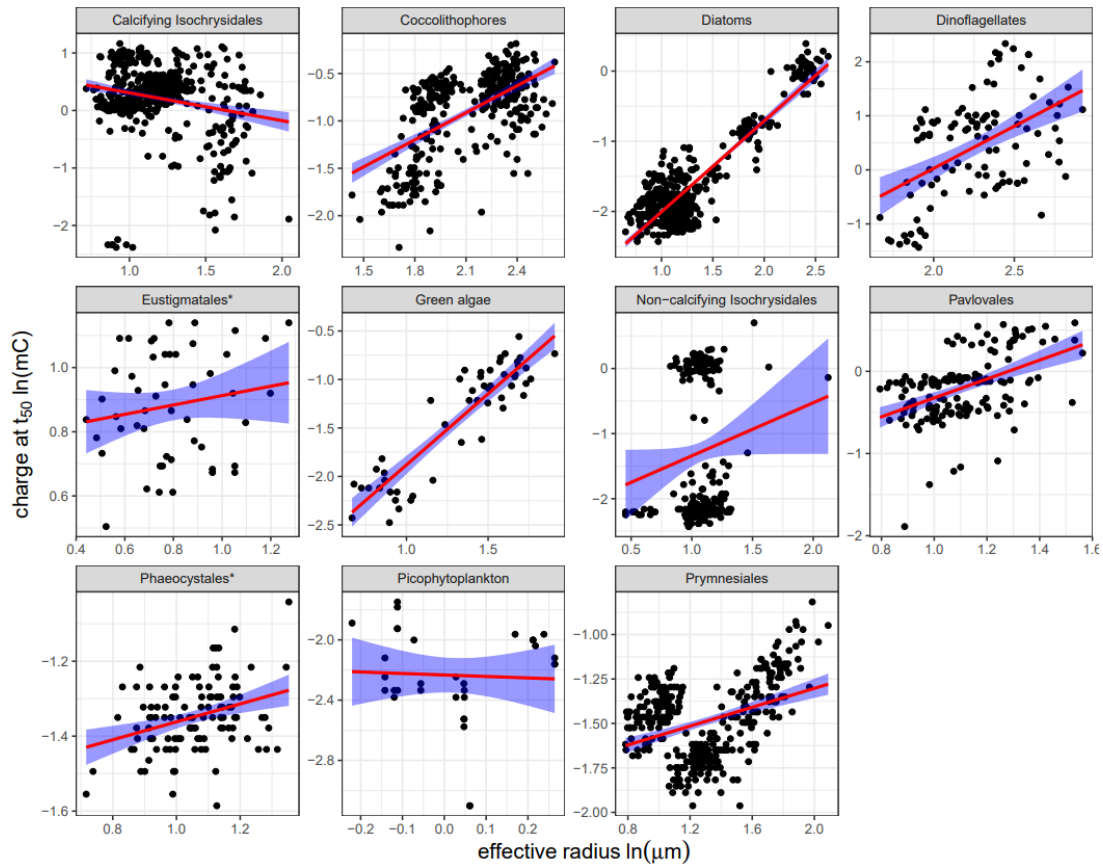
Figure S7: Scatterplots of natural log charge at t_{50} (mC) against natural log effective cell radius (μm) of cells measured for each phytoplankton group in this study, following the balancing of strain representation per group (n = 2277). The red line indicates the overall slope of the allometric relationship modelled for each level of grouping, and the blue shading is a visual representation of the 95% confidence of this fit. See Table S11 for the coefficients of each individual model fit, and respective p values. *denotes groups that were just represented by a single species.

967
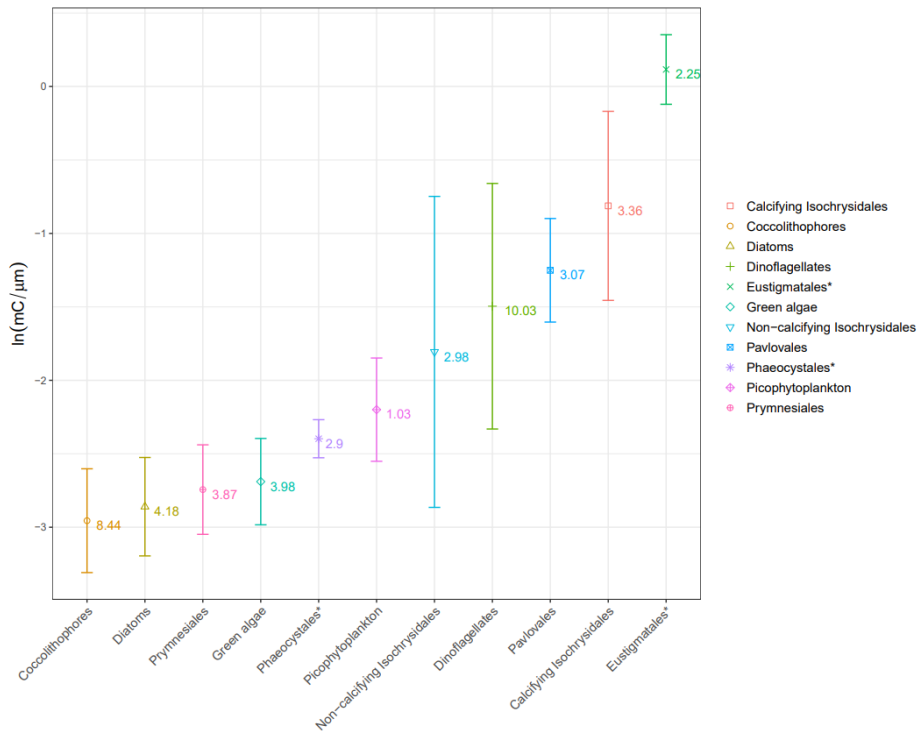
Figure S8: Comparison of per group natural log transformed mean of size normalised charge at t_{50}. Data points represent the mean value for each group and the error bars are for standard deviation, following balancing the representation of the individual strains within each group. The labelled numbers alongside the data points represent the mean effective radius for each of the groups. *denotes groups that were just represented by a single species.
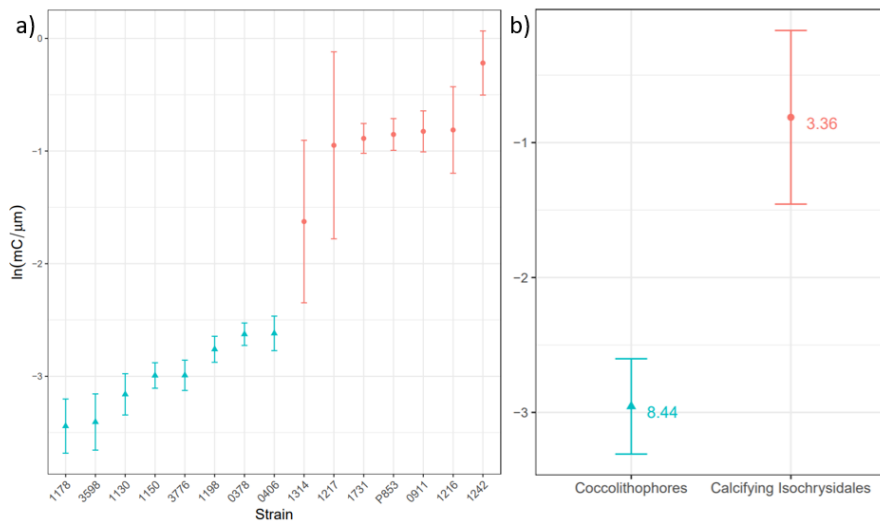
Figure S9: **(a)** Comparison of natural log size normalised charge at t_{50} across the different strains of "Coccolithophore" (blue) and "Calcifying Isochrysidales" (red) **(b)** Comparison of natural log size normalised mean charge at t_{50} the group level for "Coccolithophores" and "Calcifying Isochrysidales". Data points represent the mean values and the error bars are for standard deviation. The labelled numbers alongside the data points represent the mean effective radius. These plots clearly demonstrate that despite their much smaller size, "Calcifying Isochrysidales" are significantly more resilient in terms of their chlorophyll *a* "switch-off".

983 **Table S1:** A list of all the 52 strains used, including their grouping (in this study), their culture collection
984 strain numbers, and their respective growth medium enrichment (see Table S2). Strain prefixes relate
985 to the respective culture collections where the strain was obtained (RCC = Roscoff Culture Collection
986 (Roscoff, France), CCAP = Culture Collection of Algae and Protozoa (Oban, UK), and PLY = The
987 Marine Biological Association (Plymouth, UK)

Group	Species detail	Strain	Synthetic seawater-based growth medium
Calcifying Isochrysidales	*Emiliania huxleyi*, non-calcified haploid	RCC 1217	K/2
Calcifying Isochrysidales	*Emiliania huxleyi*, morphotype A, light -moderately calcified	RCC 911	K/2
Calcifying Isochrysidales	*Emiliania huxleyi*, morphotype A, moderately calcified	RCC 1731	K/2
Calcifying Isochrysidales	*Emiliania huxleyi*, morphotype A/R, over-calcified with bulky centre	PLY 853	K/2
Calcifying Isochrysidales	*Emiliania huxleyi* morphotype A/R, over-calcified shields	RCC 1216	K/2
Calcifying Isochrysidales	*Emiliania huxleyi*, non-calcified diploid	RCC 1242	K/2
Calcifying Isochrysidales	*Gephyrocapsa oceanica*	RCC 1314	K/2
Coccolithophores	*Calcidiscus leptoporus* (1)	RCC 1130	K/2
Coccolithophores	*Calcidiscus leptoporus* (2)	RCC 1150	K/2
Coccolithophores	*Calyptrosphaera sphaeroidea*	RCC 1178	K/2
Coccolithophores	*Chrysotila dentata* (1)	PLY 378	K/2
Coccolithophores	*Chrysotila dentata* (2)	PLY 406	K/2
Coccolithophores	*Coccolithus braarudii*	RCC 1198	K/2
Coccolithophores	*Coccolithus pelagicus*	RCC 3776	K/2
Coccolithophores	*Scyphosphaera apsteinii*	RCC 3598	L1
Diatoms	*Nitzschia closterium*	RCC 81	K
Diatoms	*Nitzschia* sp.	RCC 80	K
Diatoms	*Phaeodactylum tricornutum*	RCC 69	K
Diatoms	*Coscinodiscus* sp.	RCC 4273	K
Diatoms	*Halamphora coffeaeformis*	CCAP 1001/2	K
Diatoms	*Minidiscus comicus*	RCC 4660	K
Diatoms	*Minidiscus variabilis*	RCC 4657	K
Diatoms	*Skeletonema japonicum*	RCC 74	K
Diatoms	*Thalassiosira pseudonana*	RCC 950	K
Diatoms	*Thalassiosira weissflogii*	RCC 76	K
Dinoflagellates	*Amphidinium carterae*	RCC 88	F/2
Dinoflagellates	*Karenia papilionacea*	RCC 6516	K
Dinoflagellates	*Lepidodinium chlorophorum*	RCC 1489	F/2
Dinoflagellates	*Heterocapsa triquetra*	PLY 717	F/2
Dinoflagellates	*Prorocentrum micans*	NIES-12	F/2
Dinoflagellates	*Prorocentrum minimum*	PLY 714	F/2
Dinoflagellates	*Scripsiella trochoidea*	PLY 632	F/2
Dinoflagellates	*Thoracosphaera heimii*	RCC 1511	K/2
Eustigmatales*	*Nannochloropsis granulata*	RCC 8	F/2
Green algae	*Chlamydomonas concordia*	RCC 1	F/2
Green algae	*Dunaliella tertiolecta*	RCC 6	K
Green algae	*Bigelowiella natans*	RCC 623	F/2
Non-calcifying Isochrysidales	*Isochrysis galbana*	CCAP 927/1	K
Non-calcifying Isochrysidales	*Isochrysis litoralis*	RCC 1346	F/2

Non-calcifying Isochrysidales	*Isochrysis* sp.	RCC 4207	K
Non-calcifying Isochrysidales	*Ruttnera* sp.	RCC 3696	F/2
Pavlovales	*Diacronema vlkianum* (1)	RCC 1546	F/2
Pavlovales	*Diacronema vlkianum* (2)	RCC 3780	F/2
Pavlovales	*Pavlova granifera*	RCC 1557	F/2
Phaeocystales*	*Phaeocystis globosa*	RCC 678	K
Picophytoplankton	*Micromonas pusilla*	RCC 1614	K
Picophytoplankton	*Ostreococcus tauri*	RCC 4221	F/2
Picophytoplankton	*Synechococcus* sp. (1)	RCC 1084	F/2
Picophytoplankton	*Synechococcus* sp. (2)	RCC 2570	F/2
Prymnesiales	*Chrysochromulina camella*	RCC 1185	K/2
Prymnesiales	*Chrysochromulina* sp.	RCC 656	K
Prymnesiales	*Prymnesium parvum*	RCC 191	K

988

989

990

Table S2: The final concentration of the components of Aquil Synthetic Ocean Water (Morel et al. 1979), used to make all of the culture growth mediums (See Table S1). For medium enrichment applied to each see the following references: K (Keller et al. 1987), F/2 (Guillard and Ryther 1962), L1 (Guillard and Hargraves 1993).

		Molar Concentration in final SOW based medias (mol dm^{-3})
	NaCl	4.20×10^{-1}
	Na_2SO_4	2.88×10^{-2}
	KCl	9.39×10^{-3}
	$NaHCO_3$	2.38×10^{-3}
Synthetic Ocean Water (SOW) based on the Aquil medium recipe	KBr	8.40×10^{-4}
	H_3BO_3	4.85×10^{-5}
	NaF	7.15×10^{-5}
	$MgCl_2.6H_2O$	5.46×10^{-2}
	$CaCl_2.2H_2O$	1.05×10^{-2}
	$SrCl_2.6H_2O$	6.38×10^{-5}

995

996

997

998

999

1000

1001

1002

Table S3. A summary of the predictor variables at the strain level, prior to balancing the dataset (i.e. variable *n* across the strains within each group).

Group	Species detail	Strain	*n*	t$_{50}$ (s)	SD t$_{50}$	Charge at t$_{50}$ (mC)	SD Charge at t$_{50}$	effective radius (µm)	SD effective radius
Calcifying Isochrysidales	*Emiliania huxleyi,* non-calcified haploid	RCC 1217	115	13.60	3.82	1.00	0.42	2.76	0.59
Calcifying Isochrysidales	*Emiliania huxleyi,* morphotype A, light - moderately calcified	RCC 911	198	16.92	1.40	1.44	0.25	3.31	0.33
Calcifying Isochrysidales	*Emiliania huxleyi,* morphotype A, moderately calcified	RCC 1731	311	16.94	0.93	1.44	0.17	3.44	0.32
Calcifying Isochrysidales	*Emiliania huxleyi,* morphotype A/R, over-calcified with bulky centre	PLY 853	158	14.97	0.91	1.12	0.14	2.64	0.22
Calcifying Isochrysidales	*Emiliania huxleyi* morphotype A/R, over-calcified shields	RCC 1216	277	16.74	2.81	1.44	0.42	3.35	0.23
Calcifying Isochrysidales	*Emiliania huxleyi,* non-calcified diploid	RCC 1242	80	21.21	2.44	2.28	0.49	2.90	0.52
Calcifying Isochrysidales	*Gephyrocapsa oceanica*	RCC 1314	132	13.65	4.98	1.05	0.78	5.12	0.52
Coccolithophores	*Calcidiscus leptoporus* (1)	RCC 1130	111	7.21	0.81	0.26	0.06	6.26	0.56
Coccolithophores	*Calcidiscus leptoporus* (2)	RCC 1150	55	10.08	0.68	0.51	0.07	10.10	0.78
Coccolithophores	*Calyptrosphaera sphaeroidea*	RCC 1178	93	6.17	0.71	0.19	0.05	5.87	0.81
Coccolithophores	*Chrysotila dentata* (1)	PLY 378	69	9.89	0.58	0.49	0.06	6.79	0.54
Coccolithophores	*Chrysotila dentata* (2)	PLY 406	106	9.83	0.58	0.48	0.06	6.60	0.62
Coccolithophores	*Coccolithus braarudii*	RCC 1198	52	11.29	0.76	0.64	0.08	10.20	0.87
Coccolithophores	*Coccolithus pelagicus*	RCC 3776	40	10.15	0.78	0.52	0.08	10.33	0.97
Coccolithophores	*Scyphosphaera apsteinii*	RCC 3598	67	8.58	0.99	0.37	0.08	11.14	1.24
Diatoms	*Nitzschia closterium*	RCC 81	59	5.28	0.78	0.14	0.05	3.22	0.34
Diatoms	*Nitzschia sp.*	RCC 80	79	5.27	0.33	0.14	0.02	3.24	0.27
Diatoms	*Phaeodactylum tricornutum*	RCC 69	95	4.77	0.27	0.11	0.01	3.28	0.34
Diatoms	*Coscinodiscus* sp.	RCC 4273	40	14.23	1.15	1.02	0.17	11.03	1.15
Diatoms	*Halamphora coffeaeformis*	CCAP 1001/ 2	39	6.05	0.59	0.18	0.04	3.58	0.73
Diatoms	*Minidiscus comicus*	RCC 4660	95	5.28	0.68	0.14	0.04	2.51	0.35
Diatoms	*Minidiscus variabilis*	RCC 4657	126	5.49	0.44	0.15	0.02	2.56	0.73
Diatoms	*Skeletonema japonicum*	RCC 74	69	6.67	0.77	0.23	0.05	2.94	0.39
Diatoms	*Thalassiosira pseudonana*	RCC 950	60	5.36	0.59	0.15	0.03	2.94	0.32
Diatoms	*Thalassiosira weissflogii*	RCC 76	49	9.15	0.71	0.42	0.06	6.52	0.73
Dinoflagellates	*Amphidinium carterae*	RCC 88	157	7.65	0.80	0.30	0.06	6.31	0.61
Dinoflagellates	*Karenia papilionacea*	RCC 6516	35	12.81	1.17	0.83	0.15	12.56	1.92
Dinoflagellates	*Lepidodinium chlorophorum*	RCC 1489	34	18.11	3.74	1.71	0.70	10.20	1.32
Dinoflagellates	*Heterocapsa triquetra*	PLY 717	62	21.21	1.82	2.27	0.38	9.29	0.80
Dinoflagellates	*Prorocentrum micans*	NIES-12	13	23.07	3.98	2.73	0.93	15.05	1.81
Dinoflagellates	*Prorocentrum minimum*	PLY 714	51	12.69	1.87	0.82	0.23	7.63	1.47
Dinoflagellates	*Scripsiella trochoidea*	PLY 632	51	38.90	5.05	7.69	1.89	11.91	1.10
Dinoflagellates	*Thoracosphaera heimii*	RCC 1511	138	20.45	2.57	2.12	0.51	6.99	0.31

Eustigmatales*	*Nannochloropsis granulata*	RCC 8	50	22.06	1.85	2.45	0.41	2.25	0.46
Green algae	*Chlamydomonas concordia*	RCC 1	107	8.38	0.90	0.35	0.08	4.32	0.66
Green algae	*Dunaliella tertiolecta*	RCC 6	17	8.85	0.84	0.39	0.08	5.24	0.62
Green algae	*Bigelowiella natans*	RCC 623	269	4.84	0.43	0.12	0.02	2.41	0.33
Non-calcifying Isochrysidales	*Isochrysis galbana*	CCAP 927/1	96	9.27	4.34	0.52	0.42	3.05	0.36
Non-calcifying Isochrysidales	*Isochrysis litoralis*	RCC 1346	75	5.10	1.76	0.15	0.17	2.68	0.51
Non-calcifying Isochrysidales	*Isochrysis* sp.	RCC 4207	48	14.20	2.94	1.05	0.33	3.13	0.90
Non-calcifying Isochrysidales	*Ruttnera* sp.	RCC 3696	70	5.30	2.23	0.16	0.21	3.04	0.37
Pavlovales	*Diacronema vlkianum* (1)	RCC 1546	103	13.22	0.32	0.87	0.04	2.82	0.39
Pavlovales	*Diacronema vlkianum* (2)	RCC 3780	49	10.90	1.11	0.60	0.10	2.81	0.33
Pavlovales	*Pavlova granifera*	RCC 1557	117	15.03	2.99	1.17	0.42	3.55	0.52
Phaeocystales*	*Phaeocystis globosa*	RCC 678	110	7.22	0.33	0.26	0.02	2.90	0.37
Picophytoplankton	*Micromonas pusilla*	RCC 1614	121	5.08	0.18	0.13	0.01	1.23	0.06
Picophytoplankton	*Ostreococcus tauri*	RCC 4221	93	4.01	0.53	0.08	0.02	1.05	0.01
Picophytoplankton	*Synechococcus* sp. (1)	RCC 1084	42	5.27	0.63	0.14	0.03	0.90	0.05
Picophytoplankton	*Synechococcus* sp. (2)	RCC 2570	8	4.49	0.20	0.10	0.01	0.92	0.07
Prymnesiales	*Chrysochromulina camella*	RCC 1185	114	7.31	0.74	0.27	0.05	5.41	0.79
Prymnesiales	*Chrysochromulina* sp.	RCC 656	107	6.96	0.39	0.24	0.03	2.66	0.28
Prymnesiales	*Prymnesium parvum*	RCC 191	172	6.00	0.29	0.18	0.02	3.58	0.39
TOTAL			**4884**						

1005

1006

1007

1008

1009

1010

1011

1012

1013

1014

1015

1016

1017

1018

1019

Table S4. A summary of the predictor variables at the strain level, with the balanced dataset (i.e. standardised *n* across the strains within each group, see Methods).

Group	Species detail	Strain	*n*	t$_{50}$ (s)	SD t$_{50}$	Charge at t$_{50}$ (mC)	SD Charge at t$_{50}$	effective radius (μm)	SD effective radius
Calcifying Isochrysidales	*Emiliania huxleyi*, non-calcified haploid	RCC 1217	80	13.89	3.60	1.03	0.40	2.77	0.68
Calcifying Isochrysidales	*Emiliania huxleyi*, morphotype A, light - moderately calcified	RCC 911	80	16.85	1.37	1.43	0.24	3.29	0.32
Calcifying Isochrysidales	*Emiliania huxleyi*, morphotype A, moderately calcified	RCC 1731	80	16.81	0.91	1.42	0.16	3.47	0.31
Calcifying Isochrysidales	*Emiliania huxleyi*, morphotype A/R, over-calcified with bulky centre	PLY 853	80	14.91	0.85	1.12	0.13	2.64	0.22
Calcifying Isochrysidales	*Emiliania huxleyi* morphotype A/R, over-calcified shields	RCC 1216	80	17.04	2.65	1.49	0.39	3.37	0.24
Calcifying Isochrysidales	*Emiliania huxleyi*, non-calcified diploid	RCC 1242	80	21.21	2.44	2.28	0.49	2.90	0.52
Calcifying Isochrysidales	*Gephyrocapsa oceanica*	RCC 1314	80	13.30	4.77	1.00	0.71	5.11	0.55
Coccolithophores	*Calcidiscus leptoporus* (1)	RCC 1130	40	7.26	0.81	0.27	0.06	6.25	0.50
Coccolithophores	*Calcidiscus leptoporus* (2)	RCC 1150	40	10.06	0.58	0.51	0.06	10.14	0.70
Coccolithophores	*Calyptrosphaera sphaeroidea*	RCC 1178	40	6.08	0.84	0.19	0.06	5.91	0.82
Coccolithophores	*Chrysotila dentata* (1)	PLY 378	40	9.95	0.57	0.50	0.06	6.88	0.57
Coccolithophores	*Chrysotila dentata* (2)	PLY 406	40	9.85	0.60	0.49	0.06	6.74	0.79
Coccolithophores	*Coccolithus braarudii*	RCC 1198	40	11.31	0.77	0.64	0.09	10.15	0.84
Coccolithophores	*Coccolithus pelagicus*	RCC 3776	40	10.15	0.78	0.52	0.08	10.33	0.97
Coccolithophores	*Scyphosphaera apsteinii*	RCC 3598	40	8.52	1.15	0.37	0.10	11.13	1.32
Diatoms	*Nitzschia closterium*	RCC 81	39	5.17	0.66	0.14	0.04	3.24	0.31
Diatoms	*Nitzschia sp.*	RCC 80	39	5.29	0.34	0.14	0.02	3.27	0.26
Diatoms	*Phaeodactylum tricornutum*	RCC 69	39	4.76	0.28	0.11	0.01	3.30	0.40
Diatoms	*Coscinodiscus sp.*	RCC 4273	39	14.26	1.15	1.02	0.16	11.04	1.16
Diatoms	*Halamphora coffeaeformis*	CCAP 1001/2	39	6.05	0.59	0.18	0.04	3.58	0.73
Diatoms	*Minidiscus comicus*	RCC 4660	39	5.19	0.68	0.14	0.04	2.49	0.36
Diatoms	*Minidiscus variabilis*	RCC 4657	39	5.47	0.42	0.15	0.02	2.46	0.25
Diatoms	*Skeletonema japonicum*	RCC 74	39	6.62	0.81	0.22	0.06	2.93	0.36
Diatoms	*Thalassiosira pseudonana*	RCC 950	39	5.35	0.59	0.14	0.03	2.96	0.35
Diatoms	*Thalassiosira weissflogii*	RCC 76	39	9.13	0.72	0.42	0.06	6.51	0.70
Dinoflagellates	*Amphidinium carterae*	RCC 88	13	7.72	0.67	0.30	0.05	6.31	0.54
Dinoflagellates	*Karenia papilionacea*	RCC 6516	13	12.64	1.46	0.81	0.18	12.44	2.12
Dinoflagellates	*Lepidodinium chlorophorum*	RCC 1489	13	19.71	3.86	2.01	0.74	10.01	1.08
Dinoflagellates	*Heterocapsa triquetra*	PLY 717	13	21.78	1.57	2.38	0.34	9.58	0.79
Dinoflagellates	*Prorocentrum micans*	NIES-12	13	23.07	3.98	2.73	0.93	15.05	1.81
Dinoflagellates	*Prorocentrum minimum*	PLY 714	13	13.06	1.68	0.87	0.21	8.14	1.77
Dinoflagellates	*Scripsiella trochoidea*	PLY 632	13	38.01	5.03	7.34	1.88	11.63	1.42
Dinoflagellates	*Thoracosphaera heimii*	RCC 1511	13	20.36	2.98	2.11	0.55	7.06	0.29
Eustigmatales*	*Nannochloropsis granulata*	RCC 8	50	22.06	1.85	2.45	0.41	2.25	0.46
Green algae	*Chlamydomonas concordia*	RCC 1	17	8.12	1.01	0.33	0.08	4.28	0.58
Green algae	*Dunaliella tertiolecta*	RCC 6	17	8.85	0.84	0.39	0.08	5.24	0.62
Green algae	*Bigelowiella natans*	RCC 623	17	4.85	0.41	0.12	0.02	2.43	0.32

Non-calcifying Isochrysidales	*Isochrysis galbana*	CCAP 927/1	48	10.09	4.19	0.60	0.41	3.04	0.38
Non-calcifying Isochrysidales	*Isochrysis litoralis*	RCC 1346	48	4.87	0.78	0.12	0.05	2.71	0.54
Non-calcifying Isochrysidales	*Isochrysis* sp.	RCC 4207	48	14.20	2.94	1.05	0.33	3.13	0.90
Non-calcifying Isochrysidales	*Ruttnera* sp.	RCC 3696	48	5.36	2.36	0.17	0.22	3.03	0.36
Pavlovales	*Diacronema vlkianum* (1)	RCC 1546	49	13.29	0.32	0.88	0.04	2.84	0.37
Pavlovales	*Diacronema vlkianum* (2)	RCC 3780	49	10.90	1.11	0.60	0.10	2.81	0.33
Pavlovales	*Pavlova granifera*	RCC 1557	49	14.96	3.15	1.17	0.44	3.56	0.47
Phaeocystales*	*Phaeocystis globosa*	RCC 678	110	7.22	0.33	0.26	0.02	2.90	0.37
Picophytoplankton	*Micromonas pusilla*	RCC 1614	8	5.08	0.21	0.13	0.01	1.26	0.04
Picophytoplankton	*Ostreococcus tauri*	RCC 4221	8	3.89	0.59	0.08	0.02	1.05	0.01
Picophytoplankton	*Synechococcus* sp. (1)	RCC 1084	8	5.26	0.55	0.14	0.03	0.90	0.05
Picophytoplankton	*Synechococcus* sp. (2)	RCC 2570	8	4.49	0.20	0.10	0.01	0.92	0.07
Prymnesiales	*Chrysochromulina camella*	RCC 1185	107	7.32	0.74	0.27	0.05	5.40	0.80
Prymnesiales	*Chrysochromulina* sp.	RCC 656	107	6.96	0.39	0.24	0.03	2.66	0.28
Prymnesiales	*Prymnesium parvum*	RCC 191	107	6.02	0.26	0.18	0.02	3.56	0.36
TOTAL			**2277**						

1022

1023

Table S5. A summary of the predictor variables at the group level, with the balanced dataset (i.e. standardised *n* across the strains within each group, see Methods). *denotes groups that were just represented by a single species.

Group	*n*	t_{50} (s)	SD t_{50}	Charge at t_{50} (mC)	SD Charge at t_{50}	effective radius (µm)	SD effective radius
Calcifying Isochrysidales	560	16.29	3.66	1.39	0.57	3.36	0.89
Coccolithophores	320	9.15	1.80	0.43	0.16	8.44	2.20
Diatoms	390	6.73	2.86	0.27	0.27	4.18	2.60
Dinoflagellates	104	19.54	9.10	2.32	2.22	10.03	3.05
Eustigmatales*	50	22.06	1.85	2.45	0.41	2.25	0.46
Green algae	51	7.27	1.92	0.28	0.14	3.98	1.29
Non-calcifying Isochrysidales	192	8.63	4.75	0.48	0.47	2.98	0.60
Pavlovales	147	13.05	2.55	0.88	0.35	3.07	0.52
Phaeocystales*	110	7.22	0.33	0.26	0.02	2.90	0.37
Picophytoplankton	32	4.68	0.68	0.11	0.03	1.03	0.15
Prymnesiales	321	6.76	0.74	0.23	0.05	3.87	1.26
TOTAL	**2277**						

1027

1028

1029

1030

1031

1032

1033 **Table S6.** Results from training the random forest using a random subset of 80% of the balanced data
1034 for the key groups only ($n = 1406$). The green highlighted grid squares indicate the number of successful
1035 categorisations for each group within the training.

		TRUE (Training)				
		Calcifying Isochrysidales	Coccolithophores	Diatoms	Dinoflagellates	Picophytoplankton
PREDICTED (Training)	Calcifying Isochrysidales	423	1	9	1	0
	Coccolithophores	4	227	24	17	0
	Diatoms	7	10	262	6	0
	Dinoflagellates	0	6	7	56	0
	Picophytoplankton	0	0	0	0	26
	RECALL	0.97	0.93	0.87	0.7	1
	PRECISION	0.97	0.83	0.92	0.81	1
	F1	0.97	0.88	0.89	0.75	1
					Overall accuracy	0.92

1036

1037 **Table S7.** Results from testing the trained random forest using a subset of 20% of the balanced data
1038 for the key groups only ($n = 1406$). The green highlighted grid squares indicate the number of successful
1039 categorisations for each group within the training.

		TRUE (Testing)				
		Calcifying Isochrysidales	Coccolithophores	Diatoms	Dinoflagellates	Picophytoplankton
PREDICTED (Testing)	Calcifying Isochrysidales	125	1	4	1	0
	Coccolithophores	0	67	3	4	0
	Diatoms	0	7	79	2	0
	Dinoflagellates	1	1	2	17	0
	Picophytoplankton	0	0	0	0	6
	RECALL	0.99	0.88	0.9	0.71	1
	PRECISION	0.95	0.91	0.9	0.81	1
	F1	0.97	0.89	0.9	0.76	1
					Overall accuracy	0.92

1040

1041

1042

1043

1044

1045

1046

1047

1048

1049

Table S8. Results from training the random forest using a random subset of 80% of the balanced data for all groups (*n* = 2277). The green highlighted grid squares indicate the number of successful categorisations for each group within the training.

		TRUE (Training)										
		Calcifying Isochrysidales	Coccolithophores	Diatoms	Dinoflagellates	Eustigmatales*	Green algae	Non-calcifying Isochrysidales	Pavlovales	Phaeocystales*	Picophytoplankton	Prymnesiales
PREDICTED (Training)	Calcifying Isochrysidales	372	0	5	0	9	7	36	32	1	0	0
	Coccolithophores	4	212	22	13	0	1	0	0	0	0	13
	Diatoms	3	10	176	8	0	13	49	2	5	0	31
	Dinoflagellates	0	5	7	54	0	0	1	0	0	0	0
	Eustigmatales*	8	0	0	0	30	0	0	0	0	0	0
	Green algae	5	1	6	1	0	11	0	0	1	0	3
	Non-calcifying Isochrysidales	19	0	29	0	0	2	42	3	2	0	0
	Pavlovales	18	0	1	0	0	0	12	84	0	0	2
	Phaeocystales*	0	0	10	0	0	0	2	1	42	0	32
	Picophytoplankton	0	0	0	0	0	0	0	0	0	29	0
	Prymnesiales	5	16	46	4	0	8	6	2	37	0	182
	RECALL	0.86	0.87	0.58	0.68	0.77	0.26	0.28	0.68	0.48	1	0.69
	PRECISION	0.81	0.8	0.59	0.81	0.79	0.39	0.43	0.72	0.48	1	0.59
	F1	0.83	0.83	0.59	0.73	0.78	0.31	0.34	0.7	0.48	1	0.64
											Overall accuracy	0.69

Table S9. Results from testing the trained random forest using a subset of 20% of the balanced data for all groups (*n* = 2277). The green highlighted grid squares indicate the number of successful categorisations for each group within the training.

		TRUE (Testing)										
		Calcifying Isochrysidales	Coccolithophores	Diatoms	Dinoflagellates	Eustigmatales*	Green algae	Non-calcifying Isochrysidales	Pavlovales	Phaeocystales*	Picophytoplankton	Prymnesiales
PREDICTED (Testing)	Calcifying Isochrysidales	110	1	2	0	5	2	11	7	0	0	0
	Coccolithophores	0	65	3	4	0	0	0	0	0	0	3
	Diatoms	0	6	55	2	0	1	16	0	0	0	4
	Dinoflagellates	1	0	2	18	0	0	0	0	0	0	1
	Eustigmatales*	1	0	0	0	6	0	0	0	0	0	0
	Green algae	4	0	2	0	0	3	0	0	0	0	0
	Non-calcifying Isochrysidales	6	0	5	0	0	2	14	1	0	0	0
	Pavlovales	4	0	0	0	0	0	2	15	0	0	0
	Phaeocystales*	0	0	4	0	0	1	0	0	14	0	7
	Picophytoplankton	0	0	0	0	0	0	0	0	0	3	0
	Prymnesiales	0	4	15	0	0	0	1	0	8	0	43
	RECALL	0.87	0.86	0.63	0.75	0.55	0.33	0.32	0.65	0.64	1.00	0.74
	PRECISION	0.80	0.87	0.65	0.82	0.86	0.33	0.50	0.71	0.54	1.00	0.61
	F1	0.83	0.86	0.64	0.78	0.67	0.33	0.39	0.68	0.58	1.00	0.67
											Overall accuracy	0.71

1059 **Table S10.** Summary of the model comparison for fitting linear models to ln(charge at t_{50}) against
1060 ln(effective radius), across the full balanced dataset (n = 2277), see Fig. 7 (Main text). The best model
1061 (lowest AIC) is the mixed model, including the random effect of grouping on the slope and intercept of
1062 the response. This indicates that there is an overall significant positive size scaling, but that the
1063 relationship differs across the groups (see Fig. S7).

	npar	AIC	BIC	logLik	deviance	Chisq	Df	Pr(>Chisq)
lm_size_dep	3	6398.24	6415.43	-3196.12	6392.24			
lmer_size_dep2	**6**	**3394.90**	**3429.29**	**-1691.45**	**3382.91**	**3009.33**	**3**	**<2.2 x 10⁻¹⁶**

Models:
lm_size_dep: ln_mC ~ ln_rad
lmer_size_dep2: ln_mC ~ ln_rad + (ln_rad | eco_group)

1064

1065 **Table S11:** Linear model output for each of the group specific relationships (see Fig. S7). Bold
1066 highlights indicate a significant allometric scaling, using p values for the slope coefficient only. 'Lower'
1067 and 'Upper' represent the 95% confidence intervals of the intercept and slope ('ln_rad') coefficients.
1068 The overall size scaling is visualised in Fig. 7 (Main text). *denotes groups that were just represented
1069 by a single species.

	(Intercept)	lower	upper	ln_rad	lower	upper	p (slope only)
Calcifying Isochrysidales	0.79	0.58	1.00	**-0.48**	**-0.66**	**-0.31**	**0.000000**
Coccolithophores	-2.91	-3.35	-2.48	**0.95**	**0.75**	**1.16**	**0.000000**
Diatoms	-3.30	-3.45	-3.15	**1.30**	**1.19**	**1.40**	**0.000000**
Dinoflagellates	-3.10	-3.83	-2.36	**1.56**	**1.24**	**1.88**	**0.000000**
Eustigmatales*	0.77	0.19	1.35	0.15	-0.56	0.85	0.680259
Green algae	-3.35	-3.88	-2.81	**1.47**	**1.07**	**1.86**	**0.000000**
Non-calcifying Isochrysidales	-2.16	-2.58	-1.73	**0.82**	**0.43**	**1.20**	**0.000040**
Pavlovales	-1.47	-2.03	-0.92	**1.15**	**0.65**	**1.64**	**0.000005**
Phaeocystales*	-1.60	-2.39	-0.82	0.24	-0.50	0.98	0.524655
Picophytoplankton	-2.23	-2.41	-2.06	-0.10	-1.31	1.11	0.872391
Prymnesiales	-1.83	-2.07	-1.60	**0.27**	**0.09**	**0.44**	**0.002990**
Overall (lmer model, see Table S10)	-1.83	-2.76	-0.91	**0.72**	**0.30**	**1.13**	NA

1070

1071 **Table S12.** A summary of the Pairwise Wilcoxon Rank Sum testing, to complement Fig. 8 (Main text).
1072 Bold text indicates a significant difference ($p < 0.05$) in the mC/µm values between the pairs.

Group1	Group2	p value (Bonferroni adjusted for nonparametric data)
Coccolithophores	**Calcifying Isochrysidales**	**0.000000**
Diatoms	**Calcifying Isochrysidales**	**0.000000**
Dinoflagellates	**Calcifying Isochrysidales**	**0.000000**
Eustigmatales*	**Calcifying Isochrysidales**	**0.000000**
Green algae	**Calcifying Isochrysidales**	**0.000000**
Non-calcifying Isochrysidales	**Calcifying Isochrysidales**	**0.000000**
Pavlovales	**Calcifying Isochrysidales**	**0.000000**
Phaeocystales*	**Calcifying Isochrysidales**	**0.000000**
Picophytoplankton	**Calcifying Isochrysidales**	**0.000000**
Prymnesiales	**Calcifying Isochrysidales**	**0.000000**
Diatoms	Coccolithophores	0.388386

Dinoflagellates	**Coccolithophores**	**0.000000**
Eustigmatales*	**Coccolithophores**	**0.000000**
Green algae	**Coccolithophores**	**0.000012**
Non-calcifying Isochrysidales	**Coccolithophores**	**0.009010**
Pavlovales	**Coccolithophores**	**0.000000**
Phaeocystales*	**Coccolithophores**	**0.000000**
Picophytoplankton	**Coccolithophores**	**0.000000**
Prymnesiales	**Coccolithophores**	**0.000000**
Dinoflagellates	**Diatoms**	**0.000000**
Eustigmatales*	**Diatoms**	**0.000000**
Green algae	**Diatoms**	**0.005731**
Non-calcifying Isochrysidales	Diatoms	1.000000
Pavlovales	**Diatoms**	**0.000000**
Phaeocystales*	**Diatoms**	**0.000000**
Picophytoplankton	**Diatoms**	**0.000000**
Prymnesiales	**Diatoms**	**0.000124**
Eustigmatales*	**Dinoflagellates**	**0.000000**
Green algae	**Dinoflagellates**	**0.000000**
Non-calcifying Isochrysidales	**Dinoflagellates**	**0.001037**
Pavlovales	**Dinoflagellates**	**0.000007**
Phaeocystales*	**Dinoflagellates**	**0.000007**
Picophytoplankton	Dinoflagellates	0.325385
Prymnesiales	**Dinoflagellates**	**0.000000**
Green algae	**Eustigmatales***	**0.000000**
Non-calcifying Isochrysidales	**Eustigmatales***	**0.000000**
Pavlovales	**Eustigmatales***	**0.000000**
Phaeocystales*	**Eustigmatales***	**0.000000**
Picophytoplankton	**Eustigmatales***	**0.000000**
Prymnesiales	**Eustigmatales***	**0.000000**
Non-calcifying Isochrysidales	Green algae	1.000000
Pavlovales	**Green algae**	**0.000000**
Phaeocystales*	**Green algae**	**0.000000**
Picophytoplankton	**Green algae**	**0.000001**
Prymnesiales	Green algae	1.000000
Pavlovales	**Non-calcifying Isochrysidales**	**0.000000**
Phaeocystales*	Non-calcifying Isochrysidales	0.056749
Picophytoplankton	Non-calcifying Isochrysidales	1.000000
Prymnesiales	Non-calcifying Isochrysidales	1.000000
Phaeocystales*	**Pavlovales**	**0.000000**
Picophytoplankton	**Pavlovales**	**0.000000**
Prymnesiales	**Pavlovales**	**0.000000**
Picophytoplankton	Phaeocystales*	0.010620
Prymnesiales	**Phaeocystales***	**0.000000**
Prymnesiales	**Picophytoplankton**	**0.000000**
Overall Kruskal-Wallis for significant effect of group		$<2.2 \times 10^{-16}$

1073

1074   **Table S13**. A summary of the Pairwise Wilcoxon Rank Sum testing, to complement Fig. 9b (Main
1075   text), showing the difference in natural ln(mC/µm) across the different *Emiliania huxleyi* strains in this
1076   study. Bold text indicates a significant difference ($p < 0.05$) in the mC/µm values between the pairs.
1077   The non-calcified diploid strain of *E. huxleyi* is significantly different to all other strains, with a higher
1078   average mC/µm.

Group 1	Group 2	*p* value (Bonferroni adjusted for nonparametric data)
Morphotype A, moderately calcified (1731)	Morphotype A, light to moderately calcified (911)	0.601538
Morphotype A/R, over-calcified shields (1216)	Morphotype A, light to moderately calcified (911)	0.051449
Morphotype A/R, over-calcified, bulky centre (PLY853)	Morphotype A, light to moderately calcified (911)	1.000000
Non-calcified, diploid (1242)	**Morphotype A, light to moderately calcified (911)**	**0.000000**
Non-calcified, Haploid (1217)	Morphotype A, light to moderately calcified (911)	0.581945
Morphotype A/R, over-calcified shields (1216)	**Morphotype A, moderately calcified (1731)**	**0.000078**
Morphotype A/R, over-calcified, bulky centre (PLY853)	Morphotype A, moderately calcified (1731)	0.526381
Non-calcified, diploid (1242)	**Morphotype A, moderately calcified (1731)**	**0.000000**
Non-calcified, Haploid (1217)	Morphotype A, moderately calcified (1731)	1.000000
Morphotype A/R, over-calcified, bulky centre (PLY853)	**Morphotype A/R, over-calcified shields (1216)**	**0.000945**
Non-calcified, diploid (1242)	**Morphotype A/R, over-calcified shields (1216)**	**0.000000**
Non-calcified, Haploid (1217)	**Morphotype A/R, over-calcified shields (1216)**	**0.001045**
Non-calcified, diploid (1242)	**Morphotype A/R, over-calcified, bulky centre (PLY853)**	**0.000000**
Non-calcified, Haploid (1217)	Morphotype A/R, over-calcified, bulky centre (PLY853)	1.000000
Non-calcified, Haploid (1217)	**Non-calcified, diploid (1242)**	**0.000000**
Overall Kruskal-Wallis for effect of *Emiliania huxleyi* strain type		**<2.2 x 10-16**

1079

1080

1081

1082

1083

1084

1085

1086

1087

1088

1089

1090

49

References

1092 Guillard, R. R. L., and P. E. Hargraves. 1993. Stichochrysis immobilis is a diatom, not a chrysophyte.
1093   Phycologia **32**: 234–236. doi:10.2216/i0031-8884-32-3-234.1

1094 Guillard, R. R. L., and J. H. Ryther. 1962. STUDIES OF MARINE PLANKTONIC DIATOMS: I.
1095   CYCLOTELLA NANA HUSTEDT, AND DETONULA CONFERVACEA (CLEVE) GRAN. Can J
1096   Microbiol **8**: 229–239. doi:10.1139/m62-029

1097 Keller, M. D., R. C. Selvin, W. Claus, and R. R. L. Guillard. 1987. MEDIA FOR THE CULTURE OF
1098   OCEANIC ULTRAPHYTOPLANKTON. J Phycol **23**: 633–638. doi:10.1111/j.1529-
1099   8817.1987.tb04217.x

1100 Morel, F. M. M., J. G. Rueter, D. M. Anderson, and R. R. L. Guillard. 1979. AQUIL: A CHEMICALLY
1101   DEFINED PHYTOPLANKTON CULTURE MEDIUM FOR TRACE METAL STUDIES 1 2 . J
1102   Phycol **15**: 135–141. doi:10.1111/j.1529-8817.1979.tb02976.x

1103

1104